A High Plains Squall Line Associated with Severe Surface Winds

JEROME M. SCHMIDT AND WILLIAM R. COTTON

Department of Atmospheric Science, Colorado State University, Fort Collins, Colorado

(Manuscript received 27 October 1987, in final form 2 August 1988)

ABSTRACT

The characteristics of a severe squall line are examined using data acquired from the 1981 Cooperative Convective Precipitation Experiment (CCOPE). The case is unusual in that the squall line was decoupled from an immediate, surface-based inflow source due to a mesoβ-scale (20–200 km) outflow pool produced by a separate mesoscale convective system. Both systems participated in the development of a mesoscale convective complex which subsequently produced sustained, severe surface winds throughout its entire life cycle. Despite the absolutely stable, presquall atmospheric boundary layer, the squall line produced radar reflectivity values of 70 dBZ and storm-induced outflow of 30 m s^{-1}. Aircraft soundings in the presquall environment suggest the storm was sustained by an elevated layer of high-valued θ_e air overriding the cold dome produced by the developing MCC.

The strongest surface winds were located upshear from the convective line and consisted of a northerly (alongline) component. Because the middle-level environmental flow was from the southwest, a simple vertical transport of middle-level momentum cannot account for the observed surface flow. The strong surface winds were primarily a result of the local surface pressure gradient associated with a mesohigh–mesolow couplet that accompanied the squall line.

The squall line also maintained a strong, quasi-steady, supercell-like cell that could be tracked by radar for several hours. The kinematic structure, derived from a multiple Doppler radar analysis, shows that significant alongline flow was also generated by the rotational characteristics of the supercell. This feature distinguishes this system from tropical squall lines and many midlatitude squall lines which are composed of transient ordinary cells.

1. Introduction

Tropical and midlatitude squall lines are often considered to be steady-state mesoscale convective systems consisting of a narrow, propagating convective line and an accompanying stratiform precipitation region which may extend horizontally for several hundred kilometers either upshear (Zipser 1969; Gamache and Houze 1982; Chong et al. 1987) or downshear (Newton 1966; Ogura and Liou 1980; Houze and Rappaport 1986; Srivastava et al. 1986) of the line. Most conceptual models of squall lines depict a multibranched updraft circulation fed by a surface-based inflow source of potentially unstable air which is lifted along an advancing outflow pool generated beneath the squall line (Newton 1966; Hane 1973; Thorpe et al. 1982; Seitter and Kuo 1983; Smull and Houze 1987). These studies show the main updraft typically tilts upshear with separate branches directed toward the leading and trailing stratiform regions, and possibly a third branch which enters the convective-scale downdrafts located within the narrow zone of high radar reflectivity. In addition, squall lines often have a middle-level, rear-to-front flow that is commonly thought to descend and subsequently enhance the surface convergence along the gust front (e.g., Newton 1966). Observations have shown this feature often exists in a shallow layer, between an opposing front-to-rear flow, with speeds generally less than 17 m s^{-1} (Smull and Houze 1987).

Typically, alongline variation in the flow and precipitation structure of the squall line is considered to be insignificant when compared to the cross-line variation (i.e., 2-D). The two-dimensional assumption is often invoked to ease computational constraints in numerical modeling experiments which, despite the simplifications, readily reproduce many observed squall line kinematic features. Under suitable conditions, the squall line may also consist of steady-state supercells (Lilly 1979) or as a combination of supercells and ordinary cells (Weisman and Klemp 1984). In these situations, variations in the alongline flow (or other parameters) might then be comparable to variations in the cross-line sense.

Radar observations of squall line precipitation structure reveal that alongline variations in convective organization often occur on the mesoβ-scale (20–200 km) (e.g., Wexler 1947). These structures have been referred to as line echo wave patterns (Nolen 1959), line segments (Houze 1977), line elements (James and Browning 1979), and bow echoes (Fujita 1981). De-

Corresponding author address: Jerome Schmidt, Dept. of Atmospheric Science, Colorado State University, Fort Collins, CO 80523.

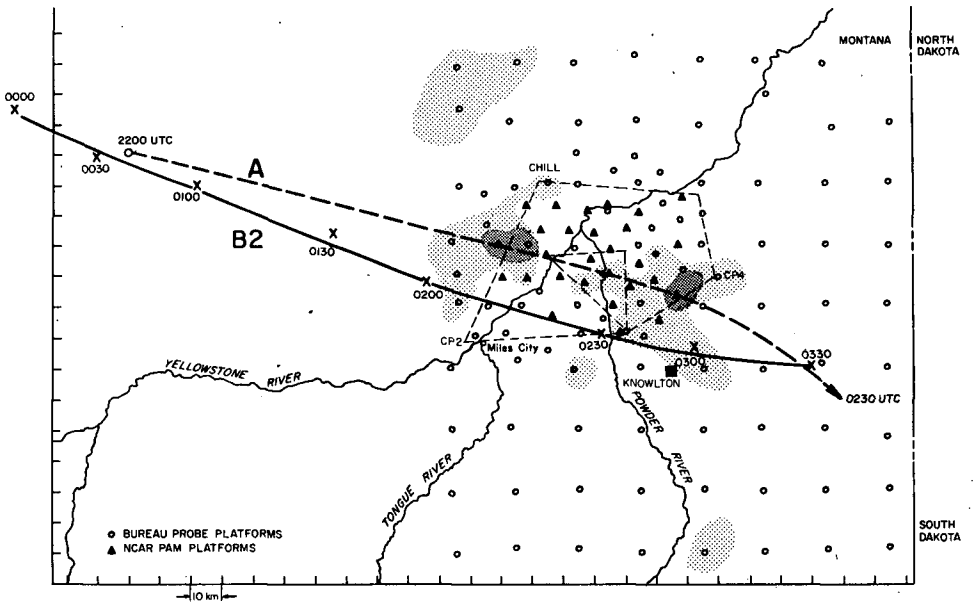

FIG. 1. Experimental setup of the CCOPE field program showing Doppler radar network (dashed polygons), surface mesonetwork (circles and triangles), and the Knowlton rawinsonde station. The tracks labeled A and B represent the movement of the storm core associated with the two mesoβ-scale systems discussed in the text. Track A was taken from Wade (1982). Light and dark stippling indicate the areas where surface wind gusts of 25 and 30 m s^{-1}, respectively, occurred from 0200 to 0330 UTC 3 August 1981, associated with the system labeled B.

tailed observations of the flow or cellular structure of these squall line entities are limited and their dynamics remain somewhat a mystery. To account for the apparent variability in convective structure that may exist along midlatitude squall lines, the line segment is regarded here as any permutation of ordinary cells and supercells enclosed within a radar reflectivity envelope that is temporarily coherent over an extended period of time.

The case examined here is noteworthy because it was associated with a number of severe wind reports. Because the squall line was embedded within a low-level stable environment associated with a MCC, it is of interest to determine which storm circulation features accounted for the strong surface outflow. We begin with a general description of the data set and analysis procedures (section 2). This is followed by a storm overview (section 3), and a presentation of the surface characteristics accompanying the squall line (section 4). These sections put the detailed Doppler radar analyses (section 5) in perspective with regard to the lifecycle of the ensuing MCC. They also document the changes in inflow characteristics that may occur with convection associated with the extensive, surface mesohighs that often accompany MCCs. A discussion of the results follows in section 6, and a summary of the case is presented in section 7.

2. Data sources and methods of analysis

The data presented here were collected during the early evening hours of 2 August 1981 from a data network assembled in southeast Montana for the CCOPE field program (Knight 1982). Figure 1 shows the distribution of surface mesonet stations, the Doppler radar array, and a rawinsonde release site used in the analyses. The surface mesonet and Doppler radar data were processed and subjectively edited for unrepresentative data, folded velocity estimates, and data gaps using the SMANAL and CEDRIC computer software described by Mohr et al. (1986). Doppler radar data were eliminated at a given grid point if the values of the quality field[1] were less than 0.6, and if the radar reflectivity was less than 10 dBZ. This second threshold was applied to reduce side lobe contamination which may arise in regions of strong radial wind and radar reflectivity gradients.

The radars used in the analyses included the University of Chicago and Illinois State Water Survey, 10-cm (S-band), CHILL Doppler radar; the NCAR, 10-cm (S-Band) CP2 and 5-cm (C-Band) CP4 Doppler radars; and the non-Doppler, Bureau of Reclamation, 5-cm (C-Band), Skywater SWR-57 radar (Fig. 1). The data were converted from radar space onto a Cartesian grid using the bilinear interpolation method described by Mohr et al. (1986). The (x, y, z) domain used in the Doppler radar analyses was typically $70 \times 90 \times 16$

[1] The quality field provides a measure of the accuracy of the interpolated fields. A value near zero is obtained if the radial velocity estimates are noise. The value approaches 1 as the spatial variability of the measured velocities decreases. See discussion by Miller et al. (1986).

km with a 1 km horizontal and 0.5 km vertical grid spacing.

Prior to synthesizing a vertical motion field, the remaining data were advected to account for the storm motion during the time interval required to sample the storm volume (Gal-Chen 1982). A nine point triangular filter using normalized weights (the Hanning filter) was then applied to smooth the velocity estimates. On horizontal scales less than 4 km, the filter and interpolation procedures will reduce the magnitude of the peak radial velocity estimates by 50% (Frank and Foote 1982). Consequently, we focus on circulation features with horizontal scales exceeding 5 km in this paper.

Vertical motion was obtained by integrating the mass continuity equation downward from storm top. The upper boundary condition was set by shifting a fractional value (arbitrarily set at 0.5) of the derived convergence in the upper-most level, one-half grid point in the vertical. Errors associated with the horizontal velocity components (usually considered to be 1–2 m s^{-1}) can be expected to produce errors in the w field of ± 5 m s^{-1}.

Rawinsonde, aircraft, and satellite data are used to analyze the storm environment and the MCC's evolution. GOES-West satellite imagery was processed using the Colorado State University IRIS system described by Green and Kruidenier (1982). Selected satellite images document the relationship between several mesoscale convective systems which impacted both the development of the squall line and the subsequent growth of the MCC.

3. System overview

a. Synoptic environment

A regional analysis of first-order National Weather Service (NWS) surface stations at 0000 UTC 3 August 1981, is shown in Fig. 2. The environment in the CCOPE region was influenced by a slow, southward moving cold front that had advanced over the northern portion of the mesonet. This front displaced a potentially unstable, high-valued θ_e airmass (>350 K) found in advance of a weak low pressure system located over central Wyoming.

The vertical structure of the prefrontal airmass indicated the potential for strong storms if a weak capping inversion could be broken (Fig. 3). A sounding released from Knowlton at 2346 UTC, shows the surface moisture was well mixed in a layer of southeasterly flow up to a capping inversion at 75 kPa (Fig. 3). Above the inversion, the flow became southwesterly resulting in a hodograph with cyclonic curvature and a vertical wind shear (computed over the lowest 6 km) of 3×10^{-3} s^{-1} (Fig. 4). This shear, coupled with a nearly dry adiabatic layer to 45 kPa, produced a bulk Richardson number of approximately 31, within the expected range for supercell storms (Weisman and Klemp 1982).

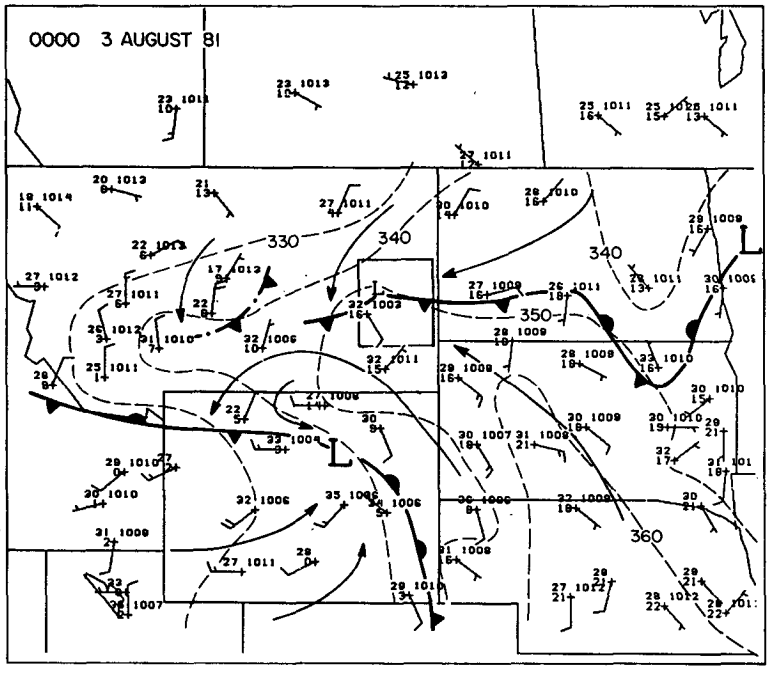

FIG. 2. Synoptic surface conditions at 0000 UTC 3 August 1981. Plotted station parameters include temperature (°C), dewpoint (°C), pressure (hPa). Dashed lines denote values of equivalent potential temperature (θ_e) at 10 K intervals.

b. *Radar and satellite precipitation characteristics*

Because of additional lifting from a weak short wave located over central Montana and continued surface heating, the inversion strength was sufficiently reduced and strong convection developed in east-central Montana. The convection organized among two primary mesoscale convective systems which subsequently passed through the CCOPE mesonet within a two hour time span (labeled A and B in Fig. 5). The first system (system A) was documented as a supercell which produced large hail and surface winds in excess of 40 m s^{-1} (Wade 1982; Weisman et al. 1983; Miller et al. 1988). This system had direct access to the high-valued θ_e air in the pre-frontal atmospheric boundary layer (ABL) as it moved east-southeastward along the cold front (Fig. 2) at 20 m s^{-1}.

The squall line (system B) was monitored by the CCOPE radars for an eight hour period between 2100 and 0500 UTC. The early precipitation structure of the squall line consisted of two well-defined line segments (labeled B1 and B2) and a trailing stratiform precipitation region (Fig. 6a). Each line segment had

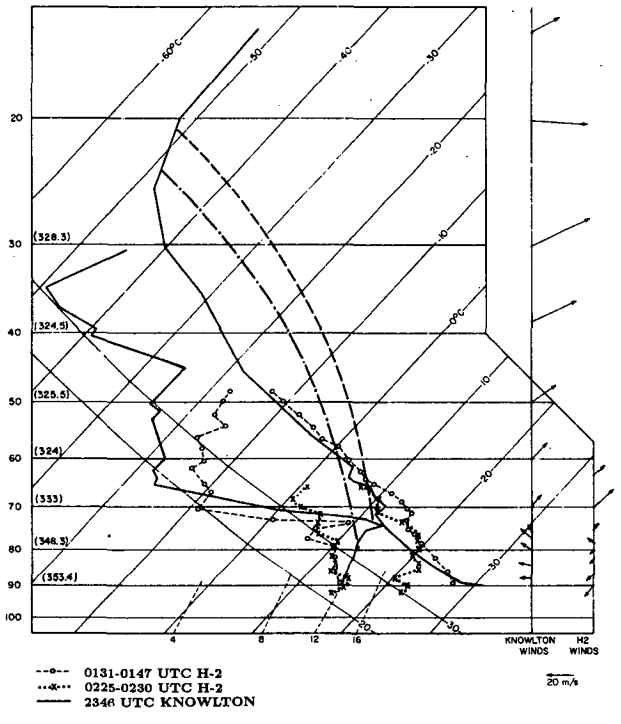

FIG. 3. Skew-T-log$P$ plot of the 2346 UTC Knowlton sounding (solid lines), and two H2 aircraft soundings near 0131 UTC (open circles) and 0225 UTC (×s). Parcel ascent based on average conditions near the surface are shown for the Knowlton (dashed curve) and the 0225 UTC H2 (dot-dashed) soundings. The winds from the Knowlton and 0225 UTC H2 soundings are plotted to the right. Numbers in parentheses represent values of θ_e derived from the Knowlton sounding and are plotted at 10 kPa intervals beginning at 90 kPa.

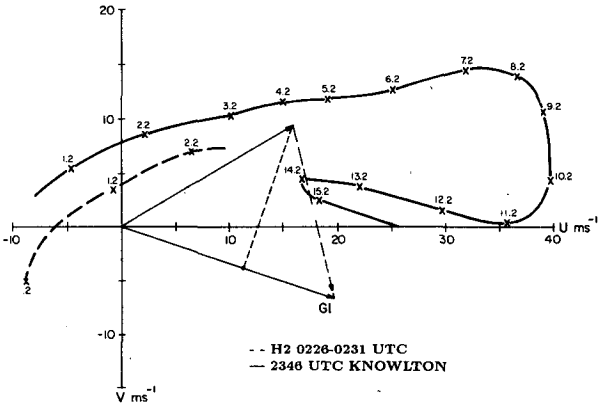

FIG. 4. Hodograph corresponding to the environmental soundings plotted in Fig. 3. Labeled ×s refer to height in km AGL. Average cell and storm motion vectors are included for system B (see Fig. 5) from 0233 to 0330 UTC.

core reflectivity values[2] between 45 and 50 dBZ and an alongline length of approximately 60–80 km. The movement was from the west and west-northwest at 21 m s^{-1} for the northern and southern line segments respectively.

During the time interval between Figs. 6a and 6b, the radar reflectivity values of B1 had weakened considerably and its convective structure could no longer be distinguished from the area of stratiform precipitation that extended toward the north (Fig. 6b). The southern line segment, meanwhile, remained strong and passed directly over the Doppler radar network where it was synchronously scanned by three Doppler radars between 0245 and 0315 UTC (Fig. 6b). Peak radar reflectivities of 70 dBZ were recorded for B2 near 0309 UTC, but these values then steadily declined as the squall line moved beyond both the Doppler and surface networks and into western North Dakota (Fig. 6c).

The cirrus cloud shields associated with A, B, and a third MCS labeled C, coalesced to meet the MCC criteria established by Maddox (1980).[3] The initial size criteria was established near the end of the Doppler radar coverage at 0315 UTC. The cloud shield reached a maximum extent near 0446 UTC (Fig. 7b) and was maintained until the system's eventual decay in central Minnesota at 1300 UTC.

As the MCC moved eastward, it produced a band of severe, straight-line winds characteristic of the derecho phenomenon (Hinrichs 1888; Johns and Hirt 1987). The derecho is defined as a convectively produced swath of damaging winds and/or wind gusts (>26 m s^{-1}) associated with an extratropical mesoscale

[2] The dBZ values from the skywater radar appeared to be underestimated by 5 to 10 dBZ.

[3] By definition the −52°C isotherm of a convective system must enclose an area of 50 000 km^2 for 6 hours to be considered a MCC.

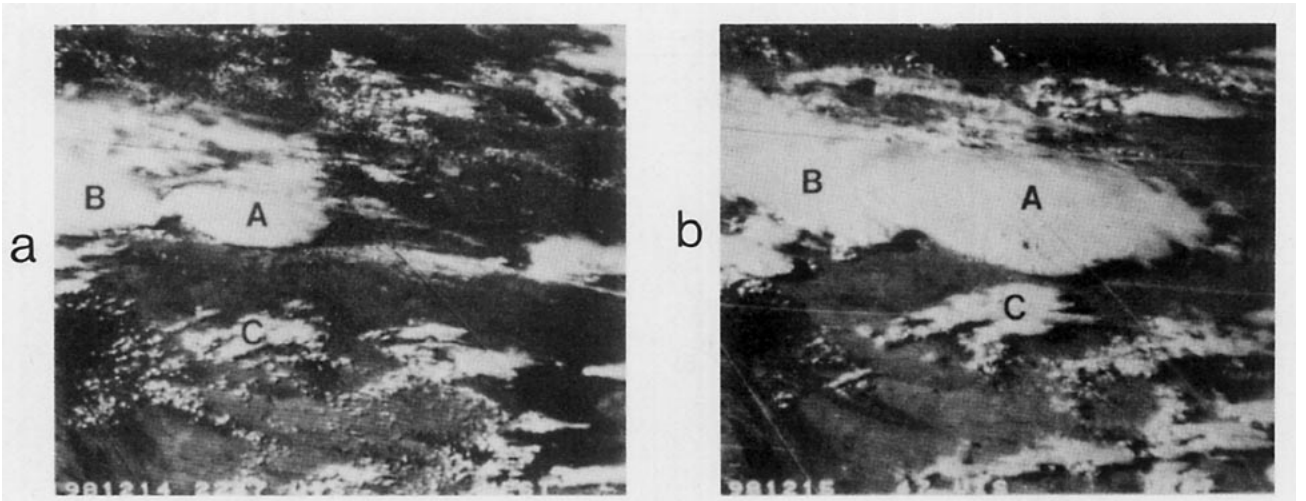

FIG. 5. Visible satellite imagery at (a) 2247 UTC 2 August and (b) 0047 UTC 3 August 1981 depicting the development and merger of several distinct mesoβ-scale convective systems which participated in the development of the MCC. Systems labeled A, B and C are discussed in the text.

convective system. The area affected by the derecho must have a major axis of at least 400 km, and no more than three hours may elapse between successive gusts and/or damage reports. In this case, the damaging winds extended from southeastern Montana to western Minnesota (Fig. 8). The derecho began with system A which produced a F1 damage in the CCOPE experimental area and western North Dakota (Weisman et al. 1983). System B produced peak gusts in excess of 30 m s^{-1} within the mesonet along a narrow band located north of the track taken by B2 (see Fig. 1). Peak surface winds of 43 m s^{-1} were later recorded in eastern South Dakota between 0830 and 1000 UTC before finally decreasing near 1300 UTC as the system entered western Minnesota.

4. Squall line environment

a. *Surface conditions*

For the remainder of the paper, we consider the environmental conditions and the convective structure of the squall line near the time of Doppler radar coverage (0245–0315 UTC). A regional surface analysis at 0300 UTC shows that the cold front had advanced to the southern border of North Dakota and, from there, trailed southwestward from system A across southeastern Montana (Fig. 9). This boundary provided an effective barrier to the warm, moist air advecting northward in advance of the synoptic-scale low in eastern Wyoming. As a result, the squall line was forced to process the cool, postfrontal surface air left in the wake of system A.

The surface conditions accompanying the squall line are shown in more detail in Fig. 10. A north–south convergence zone, of magnitude 10^{-3} s^{-1}, marked the boundary between the easterly, postfrontal airflow and the convectively induced outflow associated with the squall line. Rapid pressure changes recorded behind the gust front resulted from the passage of the 7 hPa mesohigh located over the northern portion of the mesonet. The resolved surface flow associated with this mesohigh was generally cross-isobaric and was strongest in the gradient to the *west* of the arc-shaped high pressure axis that extended beneath the line (Fig. 10b). The peak surface flow (>22 m s^{-1}) was located near the eastern portion of the wake-low (e.g., Fujita 1955; Johnson and Hamilton 1988) near (60, 0) and consisted, primarily, of a northerly, alongline component (compare Figs. 10c, d with 10b).

It is evident from the θ_e values within the mesonet, that middle-tropospheric air surfaced approximately 20–40 km upshear from the leading convective region of the squall line along a narrow east–west band near $y = -30$ (Fig. 10e). This indicates that middle-level air was transported downward without significant mixing in mesoscale downdrafts or weak convective-scale downdrafts embedded within the trailing stratiform region of the storm. This is consistent with Knupp's (1987) finding that downdrafts originating at middle-levels generally exhibit slower descent rates and reach the surface well behind the leading edge of the convective cells.

b. *Vertical airmass structure*

Data obtained by the Wyoming King Air during the period 0200–0250 UTC, revealed a two-layer structure in the low-level, presquall air mass. This aircraft performed several flight legs parallel to and immediately east of the squall line at a constant altitude of 1 km Above Ground Level (AGL) prior to performing a descent sounding that began at cloud base (z = 3 km AGL). The dominant feature of the 0225–0230 UTC aircraft sounding was the stability of the presquall ABL

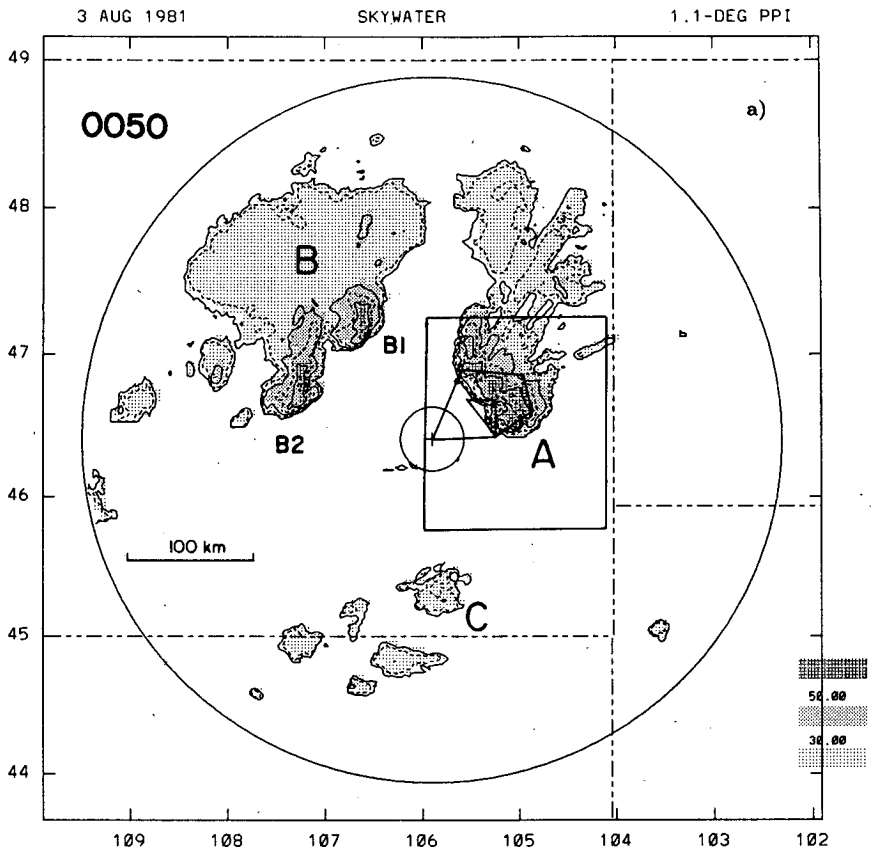
3 AUG 1981
SKYWATER
1.1-DEG PPI
0050
a)
B
B1
B2
A
C
100 km
49
48
47
46
45
44
109
108
107
106
105
104
103
102

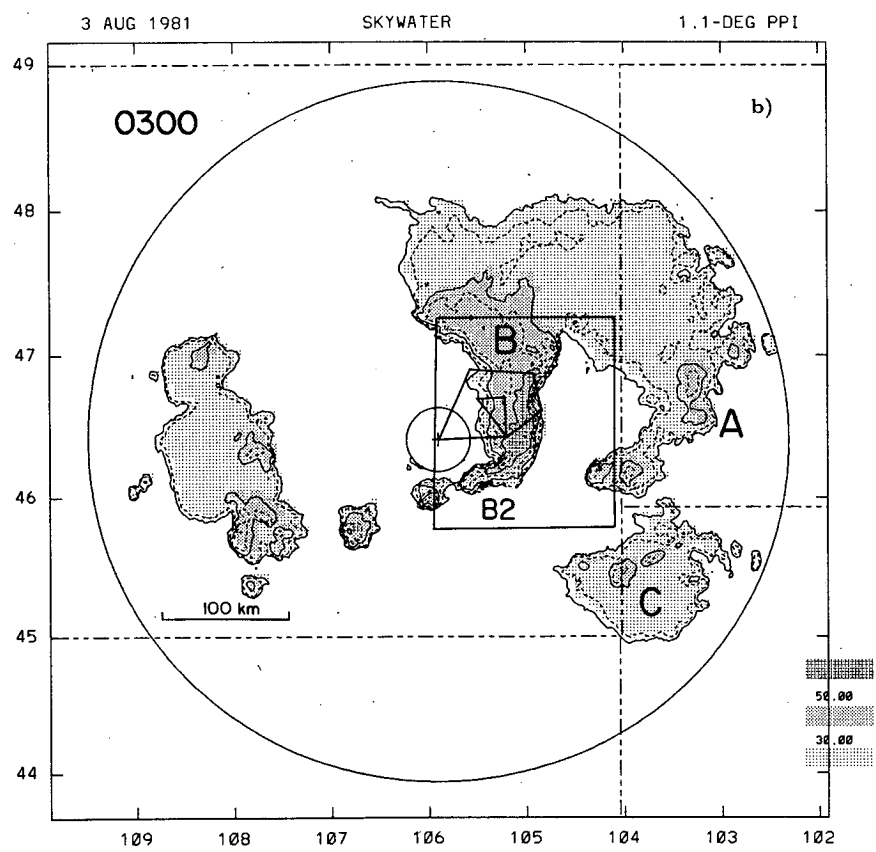
3 AUG 1981
SKYWATER
1.1-DEG PPI
0300
b)
B
A
B2
C
100 km
49
48
47
46
45
44
109
108
107
106
105
104
103
102

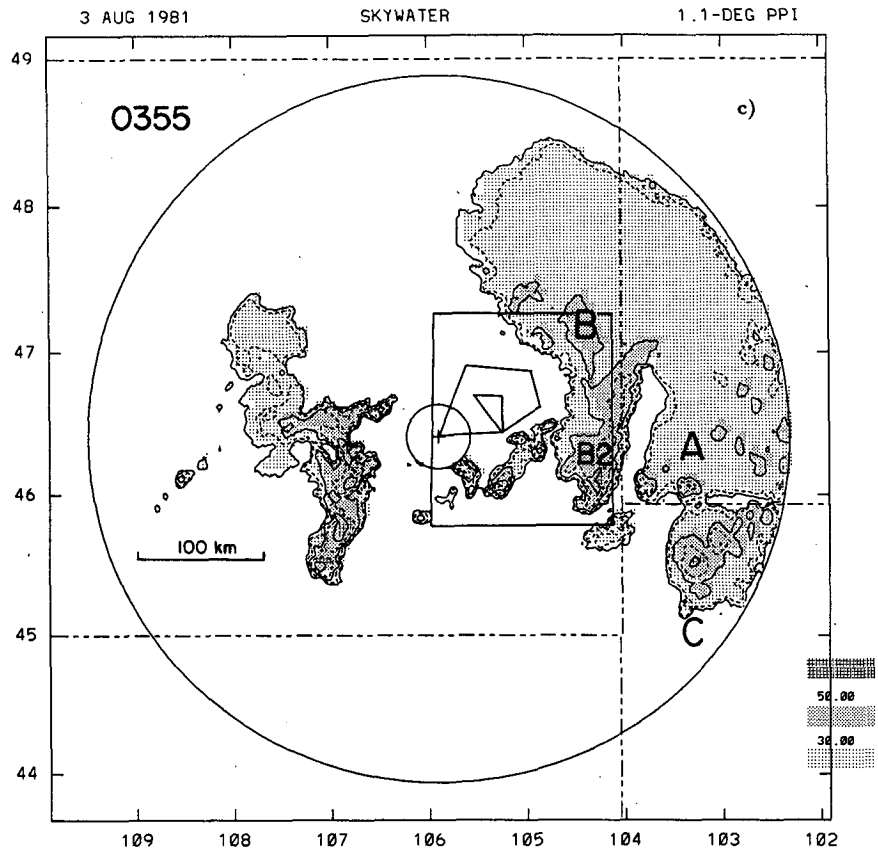

FIG. 6. Horizontal middle-level radar reflectivity cross sections at 0050, 0300 and 0355 UTC 3 August 1981 obtained from the SKWR 5 cm radar. Labeling of the major storm systems as in Fig. 5. The dashed lines depict the state boundaries. The large circle represents the 275 km range of the radar. The rectangle in eastern Montana represents the CCOPE mesonetwork and the polygons represent the Doppler radar array. Storm labels B1 and B2 are discussed in the text.

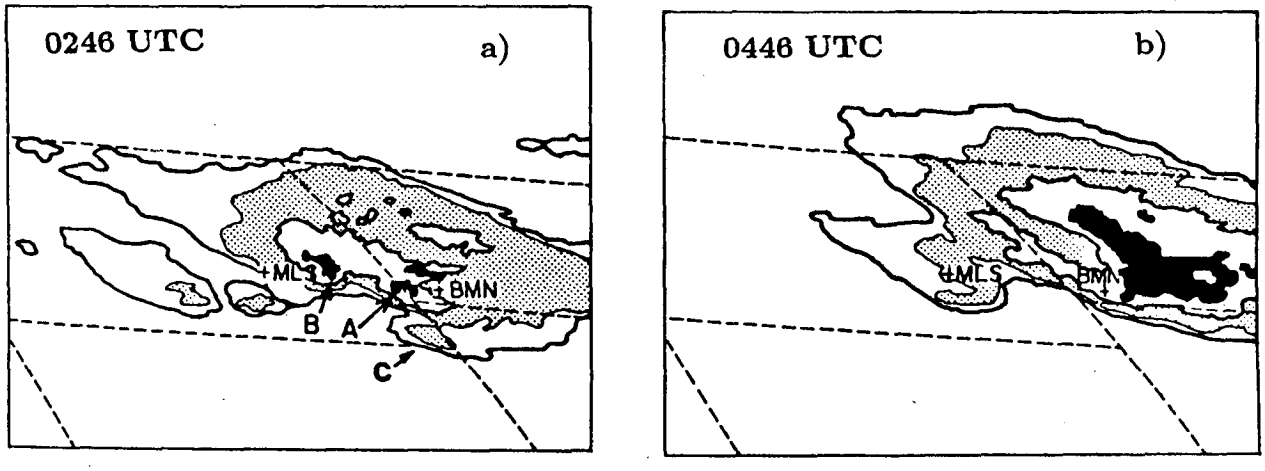

FIG. 7. Infrared satellite imagery depicting the growth of the MCC. IR isotherms enclosing −40°, −50° (shaded), −55°, −60° (black) and −65°C are shown. MLS and BMN denote radar sites at Miles City, Montana, and Bowman, North Dakota. The diameter of the system at 0446 UTC is approximately 500 km. (Figure courtesy of Pat Laybe and Ray McAnelly.)

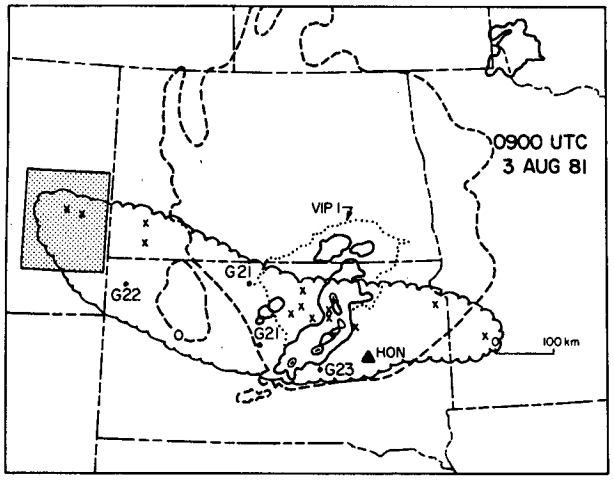

FIG. 8. Low-elevation radar PPI from Huron, South Dakota (HON) at 0900 UTC 3 August 1981 showing VIP levels 1–4. Heavy dashed line shows −32° IR contour at 0900 UTC. Severe weather occurring from 0000–1300 UTC was reported at the locations marked '×' (in *Storm Data*). Additional wind reports (courtesy of Robert H. Johns) are plotted in m s^{-1}. The stippled region outlines the CCOPE mesonet and the scalloped region encloses the area affected by the derecho.

(Fig. 3). Surface air parcels within the cool air were 6°C negatively buoyant at the lifted condensation level, a value several degrees larger than typically encountered at cloud base for High Plains storms (Marwitz 1973). Thus a favorable vertical pressure gradient would have been required to raise these parcels approximately 2.5 km before they could contribute positive buoyancy to the updraft.

A time–height sequence of aircraft derived θ_e and wind provides a more revealing depiction of the pre-squall environment and storm inflow (Fig. 11). Data obtained during the ascent to cloud base revealed a deep, well-mixed layer of west-southwesterly flow and high-valued θ_e air (>342 K) (Fig. 11 between 0220 and 0226 UTC). The θ_e values lowered sharply as the aircraft turned to the east and into clear air (near 0227 UTC), but then gradually recovered ~25 km to the east of the squall line prior to a third penetration of the low-level stable layer (Fig. 11 between 0227 and 0229 UTC). We infer from this flight segment, and other penetrations of the stable layer (see Fig. 11 at 0202, 0215, 0229 and 0233 UTC), that the inflow was confined to a shallow, elevated, high-valued θ_e layer that was lifted in a narrow zone immediately to the east of the squall line. This structure suggests a decoupling of the convective-scale updrafts from a source within the stable, presquall surface layer.

5. Doppler radar analysis

An analysis of the Doppler radar-derived flow is presented for the southern line segment (B2). Our primary objectives are to document the three-dimensional characteristics of this squall line and to determine which circulation features contributed to the observed surface wind characteristics noted in Fig. 10. For display purposes, we have chosen an analysis at 0303 UTC, but the discussion will include relevant infor-

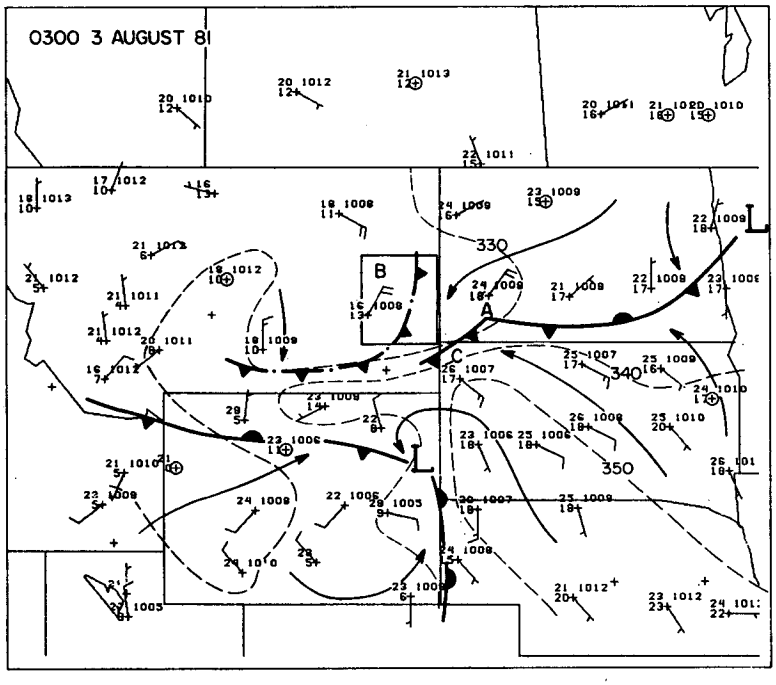

FIG. 9. As in Fig. 2 except for 0300 UTC.

mation derived from separate analyses at 0245, 0248 and 0310 UTC.

a. Precipitation structure and evolution

We use a more detailed analysis of the precipitation structure to provide additional insight in the convective organization of the line segment. The precipitation morphology of B2 is shown for a 45 min time interval in Fig. 12. The convective structure shows a division of cells into groups consisting of ordinary cells or supercells (e.g., Browning 1977). The ordinary cells were prominent along the southern portion of the bow-shaped line segment where a series of separate cell families (labeled F1, F2 and F3) formed at regular time intervals of approximately 25 minutes. These cell families formed along the advancing outflow boundary and, by maturity, formally redefined the leading edge of the line segment. During the time interval of Fig. 12, this discrete redevelopment accounted for 50% of the observed movement of the line segment.

The vertex of the bow echo was occupied by a large convective cell that sustained radar reflectivity values between 64 and 70 dBZ (labeled G1 in Fig. 12). This echo was maintained by a series of discrete convective impulses that formed in the forward overhang on the cell's southeast flank. These impulses typically formed relative maxima in the radar reflectivity field before subsequently losing their identity as they descended on the northwest flank of G1's high reflectivity envelope. This evolution resulted in a net translation of G1 to the right of the mean flow within the middle troposphere.

There were considerable differences in the areal coverage, vertical development and strength of G1's radar echo compared to the other convective cells within the line segment. A vertical cross section through G1 at 0303 UTC shows the storm top extended beyond 15.5 km AGL (Fig. 13a). Radar reflectivity values exceeding 55 dBZ were suspended above a bounded weak echo region (BWER) near $x' = 2$ (labeled V1 in Fig. 13a). A second, recently formed BWER (V2) was also evident near $x' = 13$. These closely spaced BWERs indicate strong vertical motion was present on this cell's eastern flank (Marwitz 1972). Though a persistent feature of G1, individual BWERs had lifetimes of 20–30 minutes.

The contrast in convective structure is illustrated with a single vertical cross section through the F2 and F3 cell families (Fig. 13b). The F2 cell, located near $x' = 18$, represents the typical structure of the cell families during the mature phase. This cell was comprised of a single, narrow, low-level precipitation core, and had a vertical development less than 13 km AGL. The strong radar reflectivity gradient on this cell's NW flank is indicative of an intrusion of the drier, middle-level environmental air. These cells typically reached limiting reflectivity values near 55 dBZ, were associated with transient (<10 min) weak echo regions, and could be easily tracked as distinct entities throughout their life cycle as they moved with the southwesterly flow aloft.

b. Kinematic structure

The observed variation in precipitation structure is also reflected in the storm-relative flow fields which we now describe. In the following figures, a storm movement of 21 m s^{-1} from 285° was subtracted from the Doppler-derived winds. This vector corresponds to the movement of G1 for a one hour time interval centered on the 0303 UTC analysis.

1) LOW-LEVEL FLOW

Three horizontal cross sections taken over the lower half of the storm show the relevant circulation features we seek (Fig. 14). At cloud base (3 km AGL), an easterly storm-relative flow entered the line segment north of G1 (Fig. 14a). This flow turned cyclonically, creating an alongline, northerly flow component behind the convective line, and a northwesterly return flow on the southern flank of G1.

Updraft strength generally exceeded downdraft strength at this level with the exception of the large downdraft located in the zone of high radar reflectivity on G1's northern flank. Peak speeds of 12 to 15 m s^{-1} were analyzed in the lower levels of this downdraft. Weaker downdrafts were analyzed along the western flank of G1 and between the two cell families F2 and F3. Due to their small size, the magnitude of these downdrafts probably suffered from the filtering used in the Doppler analysis.

2) MIDDLE-LEVEL FLOW

The prominent circulation feature at 4.5 km AGL was the confluence zone that formed in the trailing stratiform region between the anticyclonic/cyclonically sheared streamlines found, respectively, on the southern and northern portions of the line segment. The cyclonic circulation was more pronounced with a closed eddy circulation evident near (73, 13). The middle-level circulation around the eddy produced a peak cross-line component of flow of 8 m s^{-1} directed toward the vertex of the bow echo. This local intrusion of postsquall environmental air into the rear of the storm appeared to be associated with the downdraft zone located on the eastern portion of the eddy. This downdraft was rooted in the strong low-level downdraft noted in Fig. 14a, and was likely sustained by middle-level mixing evident within the confluence zone.

A final cross section at 7.5 km reveals three distinct changes in the storm-relative flow (Fig. 14c). Both the westerly rear-to-front and northerly flow components were absent at, and above, this level of the storm. The predominant southeasterly flow represented the southwesterly, ground-relative inflow noted in section 4. We infer from a comparison of the three horizontal cross

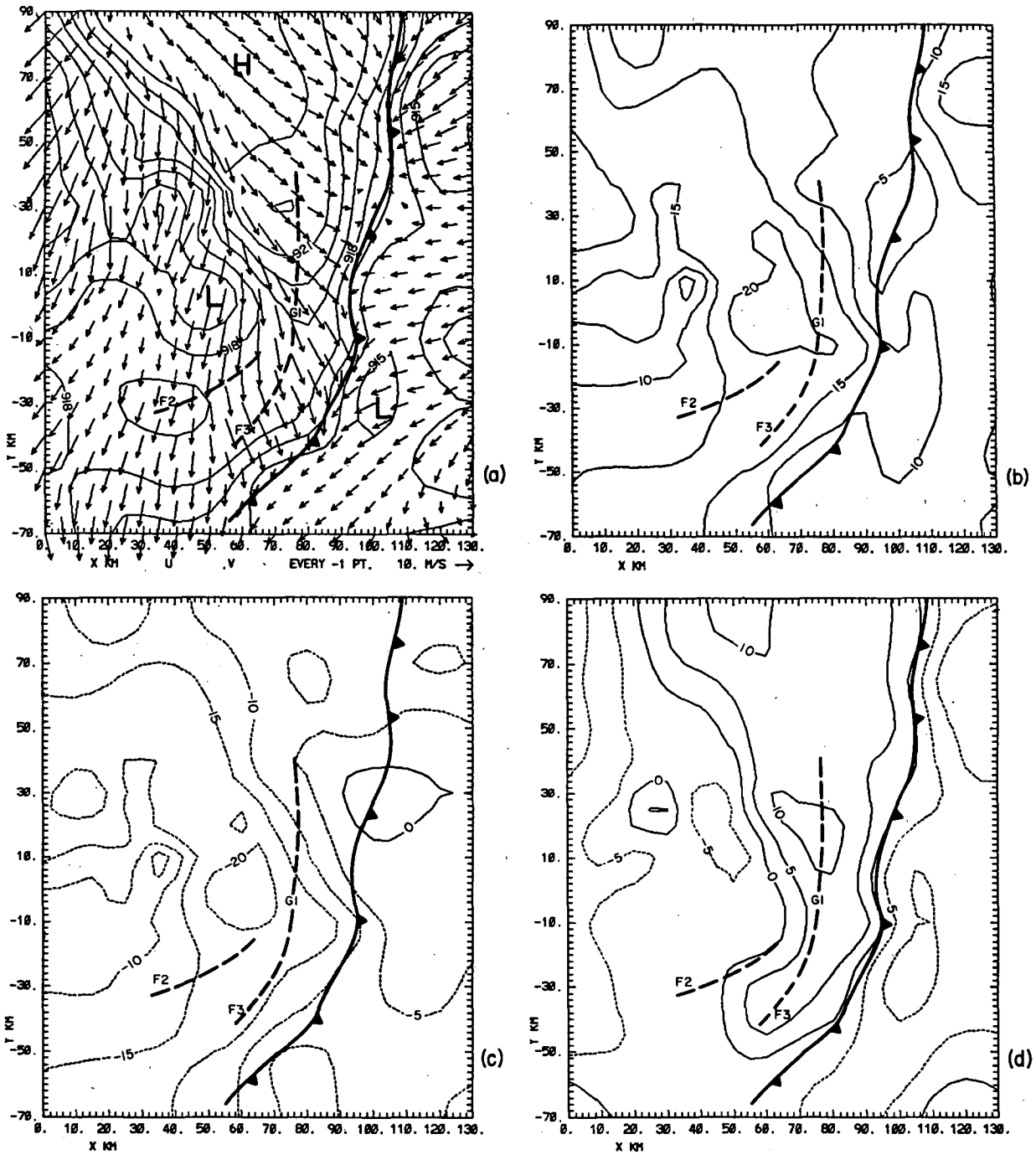

FIG. 10. Objectively analyzed surface parameters derived from the CCOPE mesonet at 0305 UTC. (a) Surface pressure, reduced to Miles City, Montana, at 1 hPa intervals and vector flow field, (b) wind speed, (c) v-component, (d) u-component contoured every 5 m s^{-1}, and (e) values of equivalent potential temperature (θ_e) contoured every 2.0 K. The bold H and L mark high and low values of pressure in (a). The bold dashed lines represent position of the convective line. The labels F2, F3, and G1 represent convective groupings discussed in the text.

sections that the $v = 0$ surface within the storm, tilted upward toward the north forming a wedge of northerly flow that undercut the opposing southeasterly flow. This is an important 3-D kinematic feature which will be discussed further in conjunction with the trajectory analyses.

Pronounced cyclonic turning was again evident near the primary updraft resulting in a positive vertical

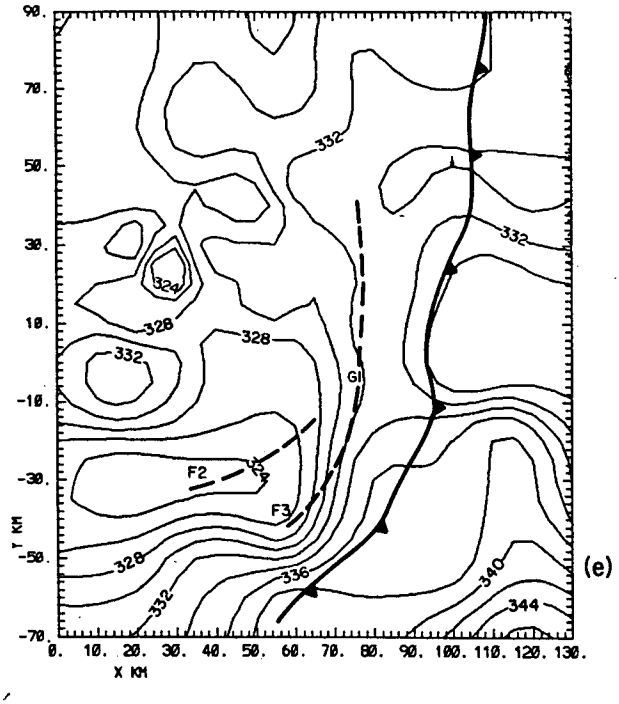

FIG. 10. *(Continued)*

component of vorticity on the order of 5×10^{-3} s^{-1} (Fig. 14c). With a few minor exceptions, this cross section also represents an upper bound to the low-level, convective-scale downdrafts. The lack of downdrafts above 7.5 km (45 kPa) probably reflects the transition to a more stable lapse rate above the midtropospheric dry adiabatic layer (Fig. 3) (referred to as the transition layer by Knupp 1987).

Another feature in Fig. 14c is the spatial separation that now appears between the dual updraft structure on G1's eastern flank and the other updrafts within the line (evident near $y = -15$). The G1 updrafts were imbedded within a common velocity envelope exceeding 12 m s^{-1} associated with two closely spaced BWERs (labeled V1 and V2 in Figs. 13a and 14b). The BWER V1 was positioned above the low-level cusp evident in the leading precipitation gradient [near (80, 0) in Fig. 14a] and was associated with the larger and stronger of the two updrafts (27 versus 21 m s^{-1} for the V1/V2 updrafts, respectively). The recently formed V2 updraft represented the latest updraft impulse to join this dominant cell group. It accounted for the extension in the 50 dBZ contour on the southern flank of G1 (Fig. 14c) and, within 10 mins, became the dominant updraft along the line.

The F2 and F3 updrafts generally reached peak speeds of 18 m s^{-1} which presumably accounted for the lower vertical development of these cells (Fig. 13b). This was the case from separate analyses at 0245, 0248 and 0315 UTC as well and indicated a consistent tendency for the strongest updrafts to regenerate within a narrow zone near the vertex of the bow-shaped line segment.

c. *Air parcel trajectories*

Trajectories were calculated to estimate the source and destination of air parcels entrained within the convective-scale downdrafts. Because the strongest surface

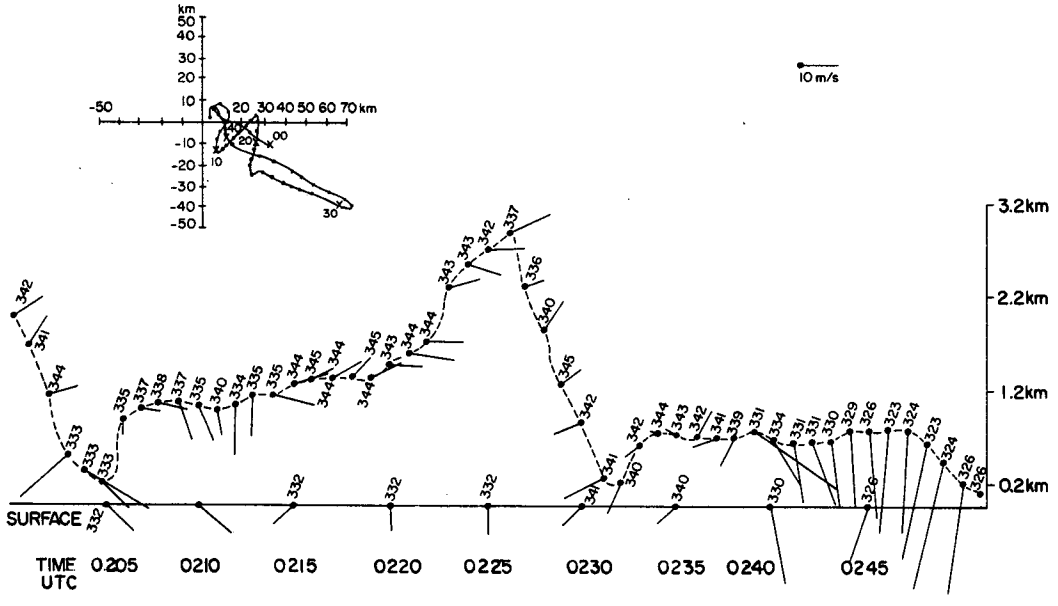

FIG. 11. Time–height cross sections from H2 from 0200 to 0250 UTC showing winds and θ_e. The dots represent one minute of flight time. Plotted surface data were taken from the objectively analyzed mesonet data below the aircraft position at 5 min intervals. The vertical axis represents height above ground level. The horizontal flight track is inset for reference at the top of the figure.

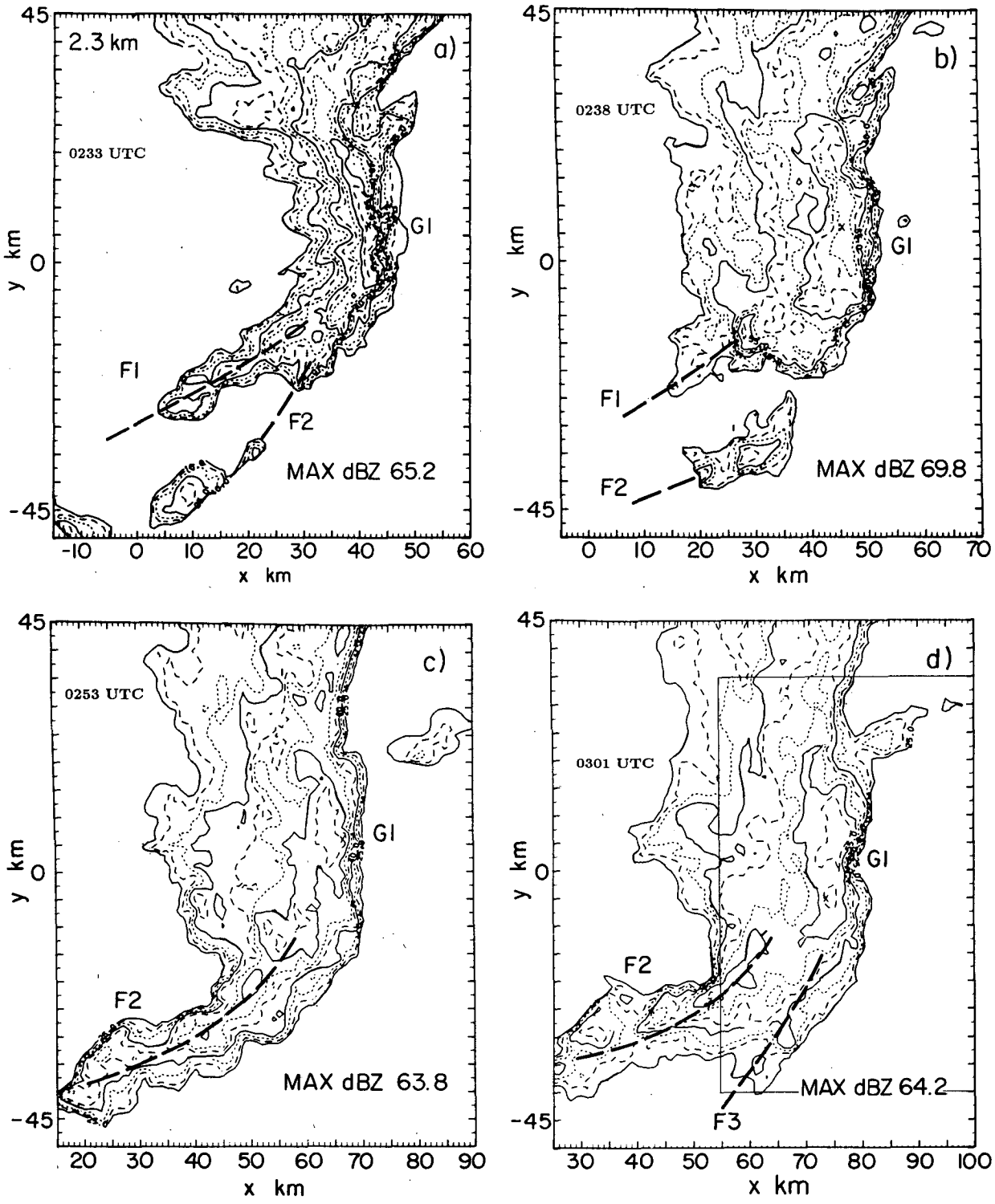

FIG. 12. Horizontal middle-level radar reflectivity cross sections from, (a) the 5 cm CP4 radar (attenuated) and the CP2 radar (b–f), showing the detailed evolution of the line segment B2 from 0233 to 0318 UTC. Contour intervals are in 5 dBZ increments beginning with 25 dBZ. Cell labeling is discussed in the text. The rectangle drawn in (d) depicts the area shown in the Doppler analysis of Fig. 14.

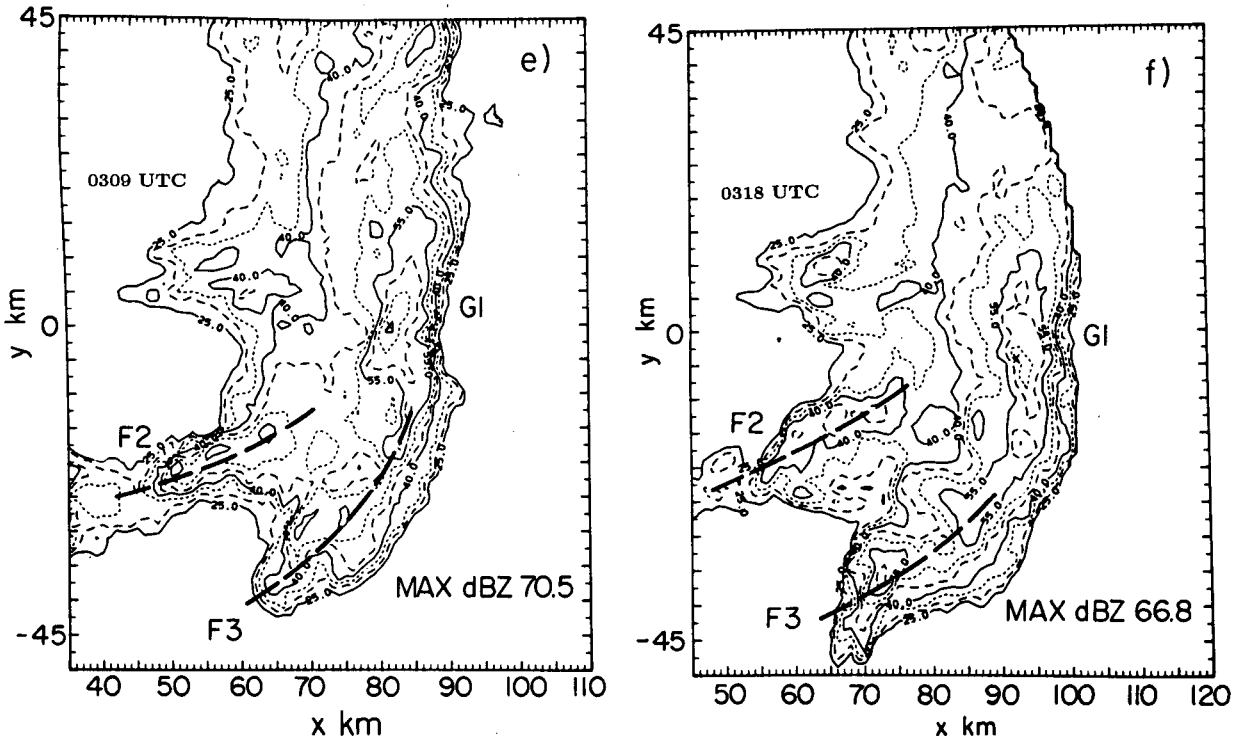

FIG. 12. *(Continued)*

winds were generally observed north of the G1 cell track (Fig. 1), we have placed our initial domains near the downdraft located on this cell's northern flank (domains outlined in Fig. 14a and b). Using the software described by Parrish and Heymsfield (1985), the trajectories were calculated both forward and backward in time from each point in the domain assuming steady state conditions at 0303 UTC. The integration used a

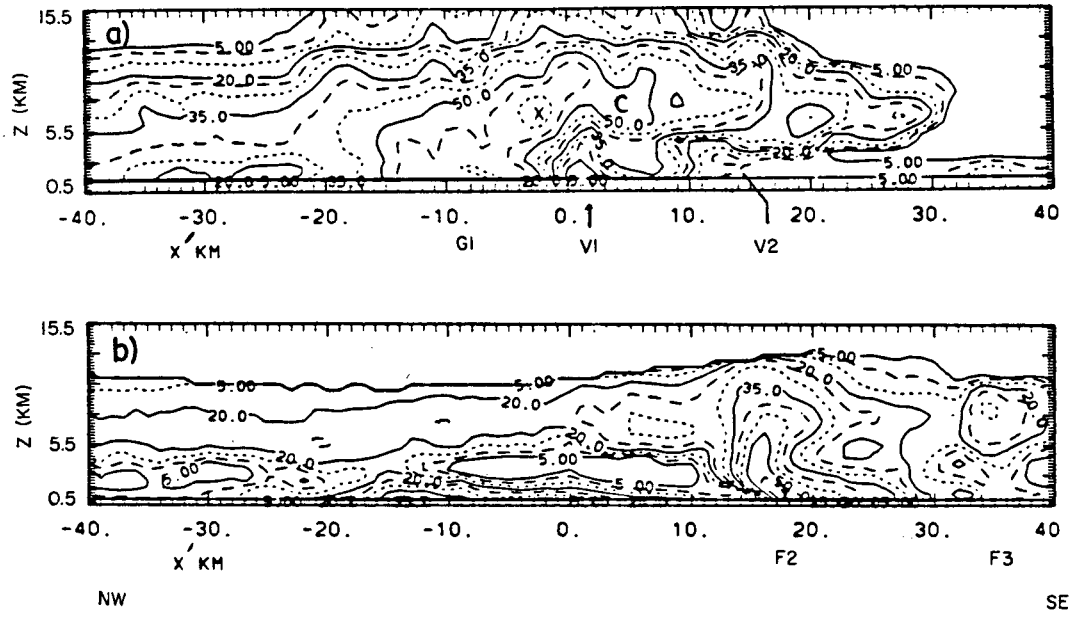

FIG. 13. Vertical cross sections depicting the structure of the (a) G1 cell group and (b) the cell families F2 and F3. Radar reflectivity is contoured at 5 dBZ intervals beginning at 5 dBZ. V1 and V2 refer to the weak echo regions discussed in the text. This cross-section was constructed by rotating the x-axis clockwise until it paralleled the discrete motion vector shown in Fig. 4 (approximately along the 166° radial).

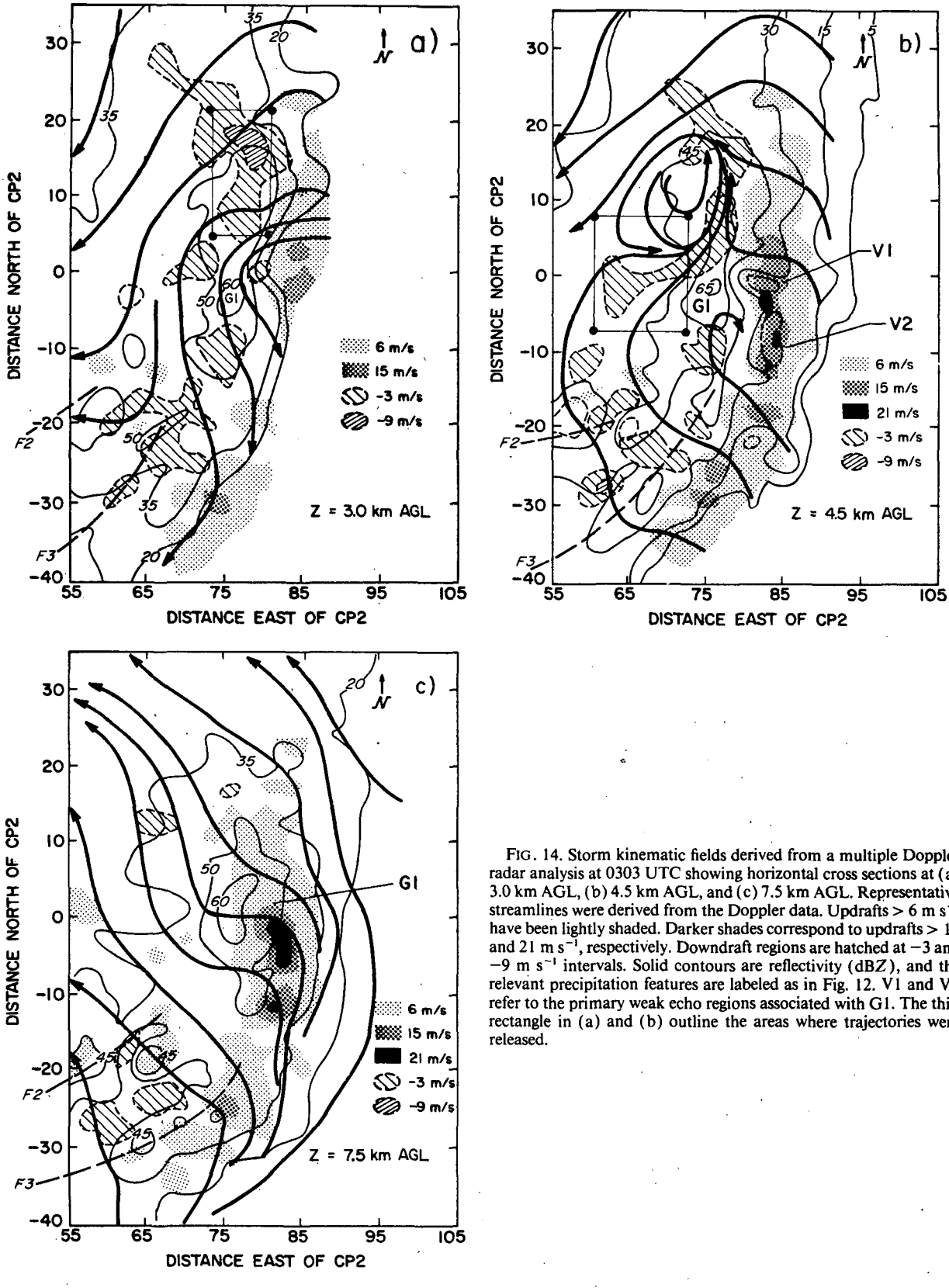

FIG. 14. Storm kinematic fields derived from a multiple Doppler radar analysis at 0303 UTC showing horizontal cross sections at (a) 3.0 km AGL, (b) 4.5 km AGL, and (c) 7.5 km AGL. Representative streamlines were derived from the Doppler data. Updrafts > 6 m s^{-1} have been lightly shaded. Darker shades correspond to updrafts > 15 and 21 m s^{-1}, respectively. Downdraft regions are hatched at −3 and −9 m s^{-1} intervals. Solid contours are reflectivity (dBZ), and the relevant precipitation features are labeled as in Fig. 12. V1 and V2 refer to the primary weak echo regions associated with G1. The thin rectangle in (a) and (b) outline the areas where trajectories were released.

10-s time step and was terminated when either a data boundary was reached or an imposed 20-min time limit expired. Due to the steady-state assumption and inherent inaccuracies in the Doppler-derived flow, the trajectories are only used to illustrate the general characteristics of the flow.

1) CONVECTIVE DOWNDRAFT TRAJECTORIES

The trajectories originating in updrafts near the leading edge of the line showed three distinct characteristics (Fig. 15). They either ascended monotonically and passed into the stratiform region (such as G), stagnated near the middle levels of the storm (F and H), or subsequently descended in downdrafts (A–E). Trajectories of the latter type, referred to as an "up–down" downdraft branch by Knupp (1987), are indicative of negatively buoyant air parcels which rise in a favorable vertical pressure gradient before increased hydrometeor loading, evaporative cooling, and cooling by melting create a net downward vertical acceleration. The majority of downdraft trajectories entrained into the primary downdraft on G1's northern flank were of the up–down variety. Originating between 1.2–4.2 km AGL, these parcels rose as high as 7.5 km AGL before rapidly descending in this downdraft. As the parcels approached the surface, they acquired a northerly flow component and showed a general tendency to exit the system toward the west.

The middle-level trajectories (F and H) typically turned anticyclonically as they merged with the middle-

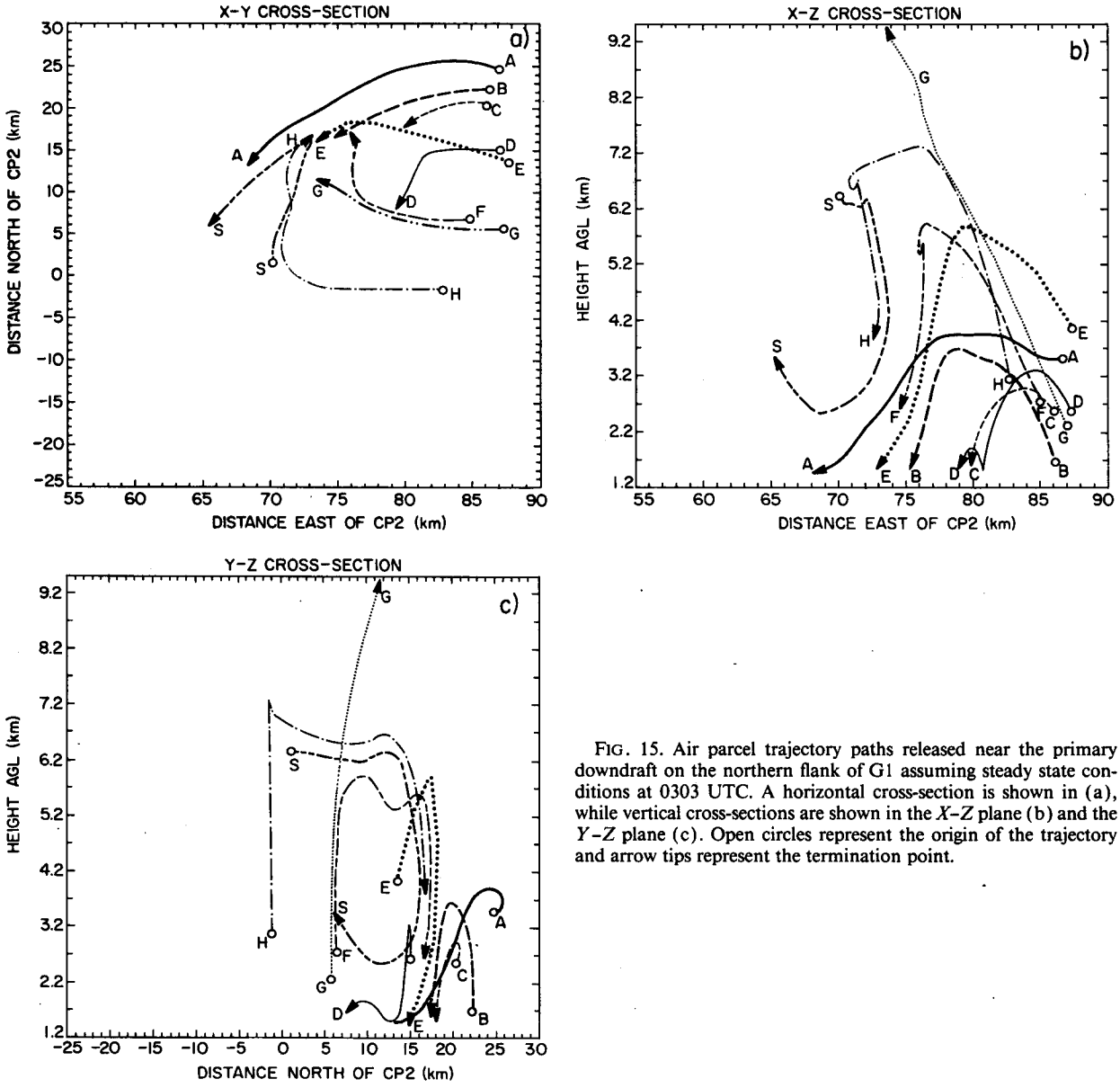

FIG. 15. Air parcel trajectory paths released near the primary downdraft on the northern flank of G1 assuming steady state conditions at 0303 UTC. A horizontal cross-section is shown in (a), while vertical cross-sections are shown in the X–Z plane (b) and the Y–Z plane (c). Open circles represent the origin of the trajectory and arrow tips represent the termination point.

level, rear-to-front flow (represented by trajectory S). Such parcels maintained a level between 5.5 and 7.0 km AGL as they progressed northward before finally descending on the western flank of the primary downdraft (Fig. 15c). This behavior reinforces the impression of mixing and alongline transport in the middle-levels of the storm suggested by the streamline analysis of Fig. 14b.

2) MIDDLE-LEVEL UPSHEAR INFLOW

We expected trajectories released in the rear-to-front flow on the storm's upshear flank (Fig. 14b) to exhibit a two-dimensional character based on the flow structure in the vertical cross sections taken normal to the line segment. Figure 16a shows the two-dimensional character of the multibranched updraft and the middle-level, rear-to-front flow common to many other observational and numerical studies of midlatitude squall lines (e.g., Newton 1950; Ogura and Liou 1980; Thorpe et al. 1982; Seitter and Kuo 1983; Smull and Houze 1987). The rear-to-front flow (shown as a positive u-component in the storm-relative flow from $x = 45$ to $x = 75$) appeared to be a coherent slab of air confined to a shallow layer between the opposing front-to-rear flow (Fig. 16b). The rear-to-front flow sloped downward across the stratiform region suggesting a vertical transport of middle-level momentum to the surface.

The two-dimensional appearance of the circulation field in Fig. 16b, however, is misleading. The middle-level trajectories which passed through this cross section (labeled M–R in Fig. 16b), illustrate this point. The trajectories reveal that the rear-to-front flow was comprised of a mixture of air parcels from several locations within the storm (Fig. 17). Trajectories originating in the middle-level southeasterly flow (M–P) showed a general tendency to turn anticyclonically into the region of rear-to-front flow where they merged with other trajectories that originated further to the west (R) and parcels arriving from the eastern flank of the line (H).

Once within the rear-to-front flow, the trajectories showed no preference to remain for extended time periods or to continue toward the leading edge of the line. Trajectory O obtained a maximum u-component of 7 m s^{-1} during a brief encounter with the rear-to-front flow (Fig. 17). Trajectory O did not carry it's acquired u-momentum toward the leading edge of the squall line; rather, it descended in downdraft, acquired a northerly flow component, and exited toward the rear of the storm. This behavior was characteristic of several parcels (such as L) upon encountering the northward-sloping $v < 0$ wedge noted in Figs. 14a, b. This suggests that the westerly, middle-level momentum was effectively transferred into an alongline component of flow within the lower levels of the line segment. This may have accounted for the displacement

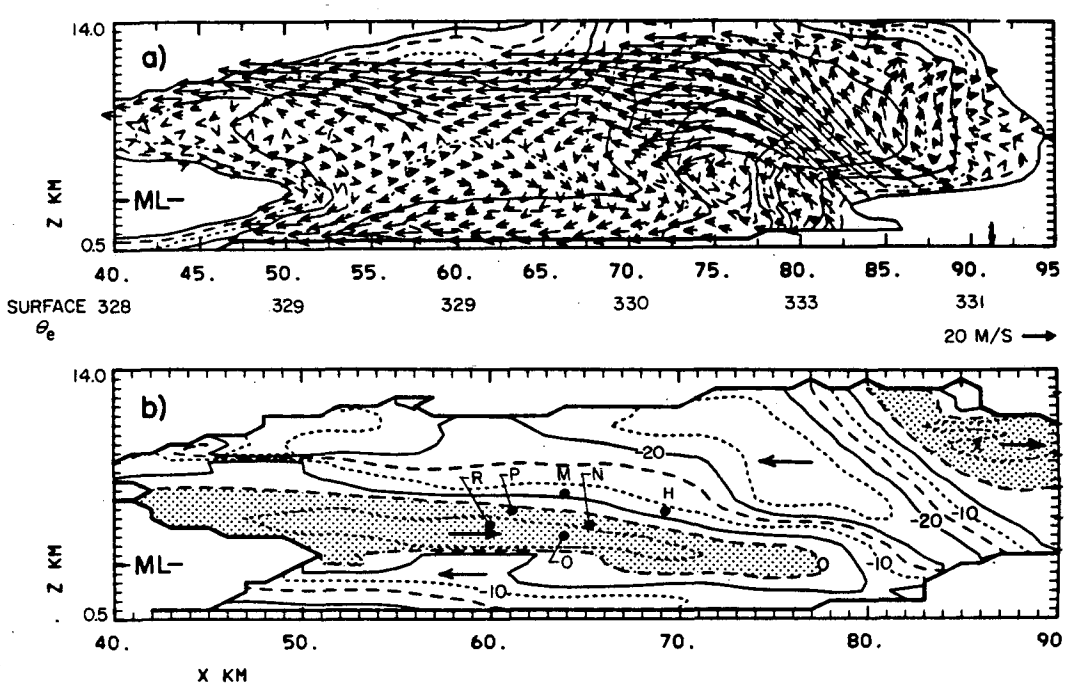

FIG. 16. Vertical cross-section taken normal to the squall line at 0303 UTC along the line $y = 0$. Storm-relative Doppler flow vectors have been superimposed on the radar reflectivity in (a). The dBZ values are contoured in 5 dBZ increments beginning with 10 dBZ. ML refers to the melting level. The u-component in (a) has been contoured at 5 m s^{-1} intervals in (b). The stippling depicts regions of positive u. The lettered dots mark the intersection of derived trajectories with this cross section. Surface θ_e values taken from objectively analyzed surface data are shown at 10 km intervals in (a). The gust front position is shown by the bold arrow at $x = 92$.

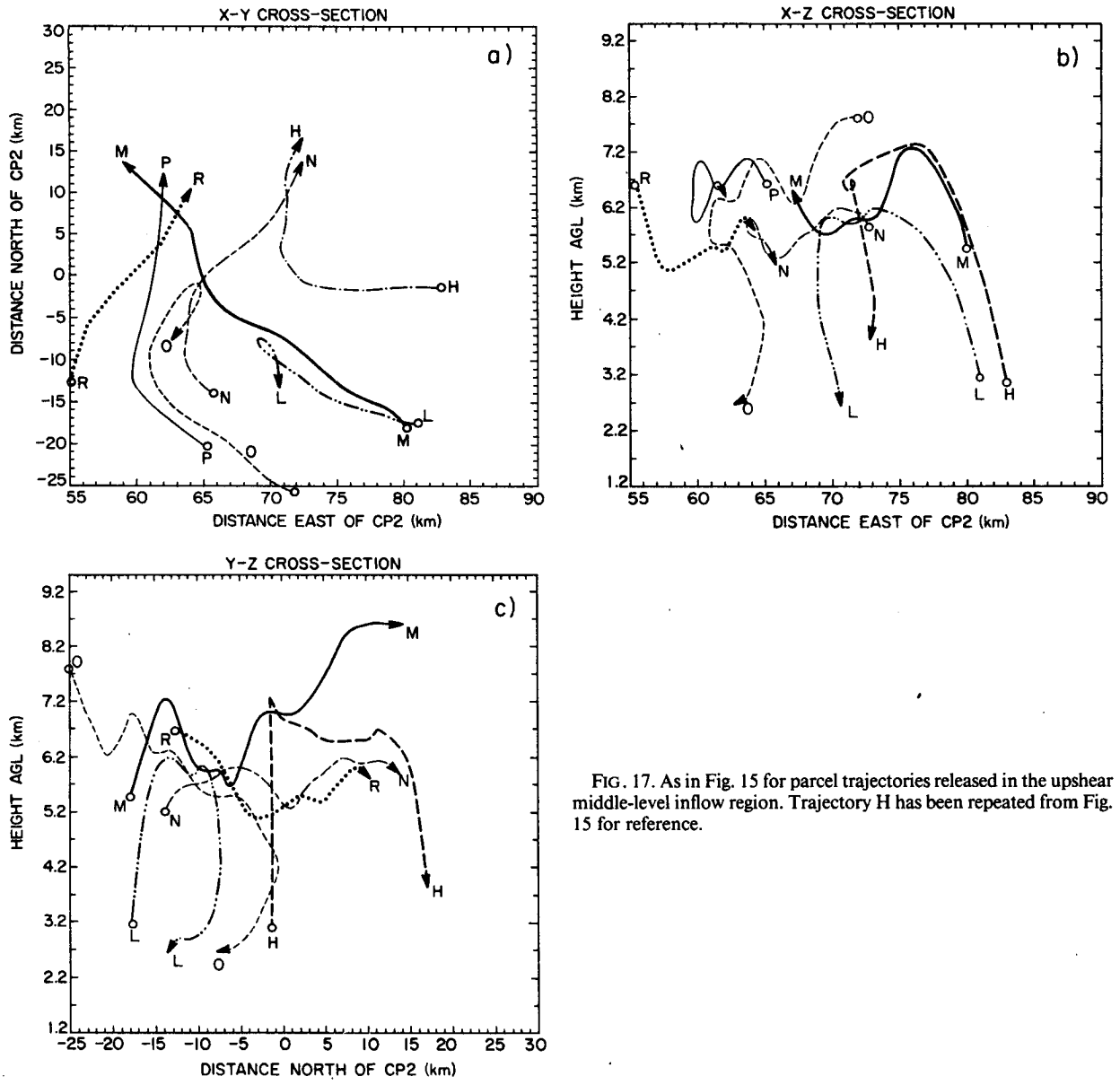

FIG. 17. As in Fig. 15 for parcel trajectories released in the upshear middle-level inflow region. Trajectory H has been repeated from Fig. 15 for reference.

of the minimum surface θ_e values to the south of the primary intrusion of rear-to-front flow rather than beneath the leading convective line (compare Figs. 14b and 10e).

d. Conceptual model

The primary mesoscale and three-dimensional storm-scale features of this line segment are summarized in a conceptual model (Fig. 19). The updrafts fed on the higher-valued θ_e air above a presquall, absolutely stable ABL. This ABL presumably resulted from a mixture of postfrontal air and convective downdraft air associated with a separate system labeled A. The elevated inflow air had characteristics of the prestorm ABL that was displaced southward by the front. We infer that overriding of low-level, moist air (depicted by the broad arrow in Fig. 19), aided in part by the synoptic scale flow fields in which the storm evolved, had a significant role in supplying adequate low-level heat and moisture to the squall line.

Considerable variation was evident in the alongline precipitation structure. The organization of the dominant, quasi-steady cell group (G1) can perhaps best be described in the continuum of storm types as an example of weak evolution (Foote and Frank 1983). This cell group had strong, closely-spaced updrafts correlated with a vertical component of vorticity on the order of 10^{-2} s^{-1}. The precipitation structure of G1 showed several supercell signatures including a

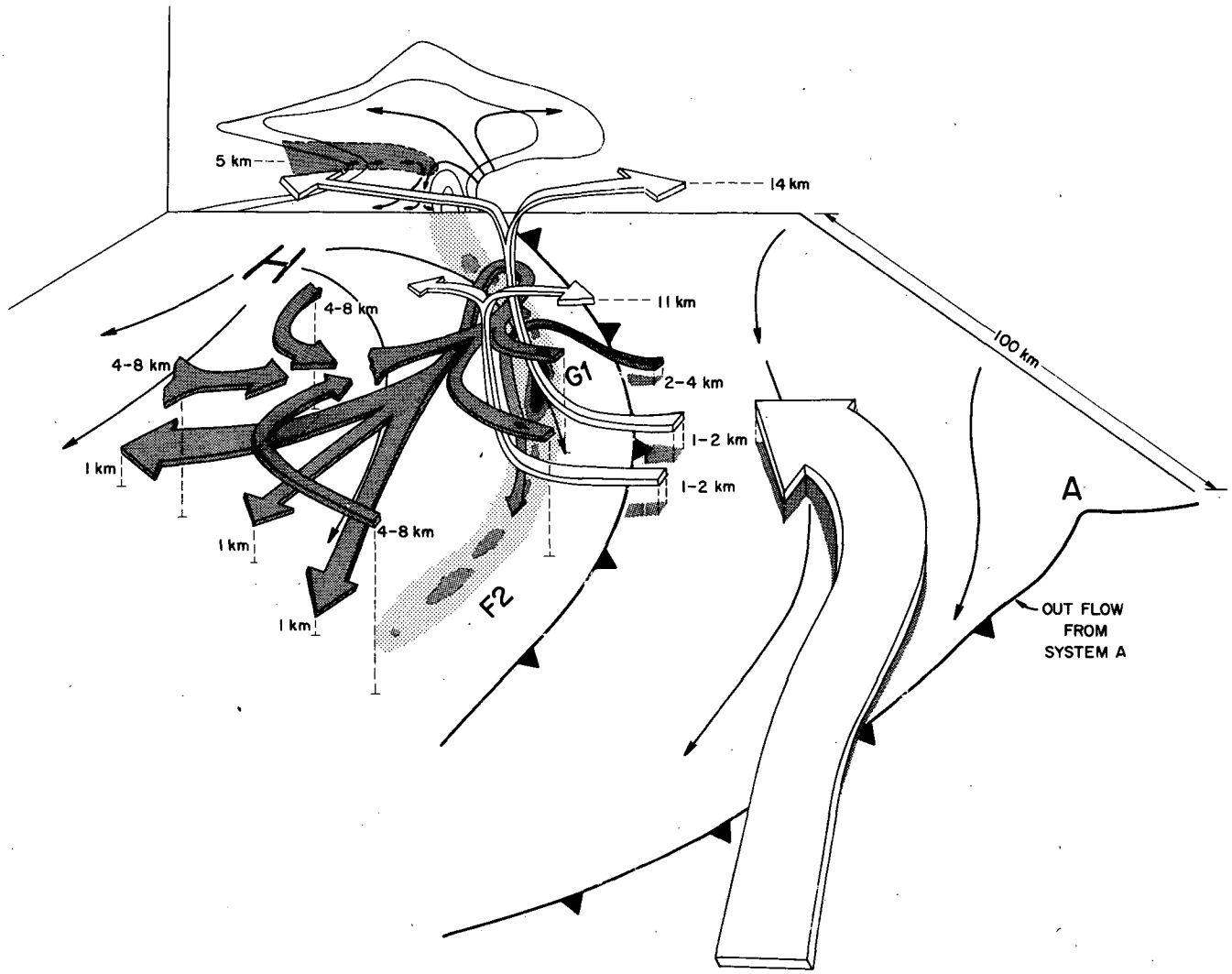

FIG. 18. Schematic depiction summarizing the 2-D and 3-D flow features discussed in the text for the 2 August 1981 CCOPE squall line showing mesoscale outflow boundaries, surface streamlines (thin arrows) convective reflectivity structure (stippled), overriding flow (bold arrow), and storm relative flow (thin ribbons). The vertical cross-section corresponds to a representative depiction of the storm core G1 and shows reflectivity (thin solid lines), schematic storm relative flow (thin arrows) and location of the middle-level upshear inflow (shaded). The bold A refers to the supercell system discussed in the text, G1 and F2 represent the cell groups along the squall line and the bold H represents the location of the surface meso-high. Labeling of the storm relative flow ribbons refers to height AGL.

BWER, a forward overhang, strong radar reflectivity values, and a resultant translation of the cell to the right of the mean wind. This cell also showed distinct structural and behavioral differences compared to other, more ordinary cells within the line segment (the F families). Primary exceptions to the supercell model were the absence of a strong, surface mesolow beneath the updraft and the presence of the middle-level, rear-to-front flow component.

Within the trailing stratiform region of the storm, there was a confluent flow which produced a narrow zone of rear-to-front flow directed toward the vertex of the bow-shaped line segment. This flow ultimately descended in the primary downdraft, located on the northern flank of G1, after mixing with the up/down downdraft trajectories which originated downshear of the squall line. These parcels acquired a northerly flow component as they descended and showed a general tendency to exit the storm to the west. The strongest surface flow was located behind the squall line where both the surface and storm-relative flow consisted of an alongline component.

6. Discussion

It is apparent that mesoscale convective systems frequently produce severe surface winds when the ABL may be absolutely stable, such as on the stable side of synoptic scale fronts or in association with MCCs (e.g., Johns and Hirt 1987). The surface winds associated

with a convective storm can result from a combination of accelerations due to the surface pressure gradient and, in cases of stronger flow aloft, to the vertical transport of middle-level momentum by convective downdrafts. The latter mechanism is typically invoked to explain the strong surface winds associated with squall lines, while for convective systems imbedded within deep stable layers, the winds may be a result of surface pressure perturbations accompanying gravity wave activity (Brunk 1949).

For the present discussion, we will determine the source of the wind maximum located near the wake mesolow where the flow was northerly or approximately parallel to the squall line axis.[4] Because the middle-level environmental flow was from the southwest, a simple argument based on conservation of middle-level momentum cannot explain the observed surface wind characteristics. Though internal gravity waves were likely in this environment, we consider the alongline flow to have been generated by the surface mesohigh and/or as a result of the rotational characteristics generated by the particularly vigorous, convective element embedded within the squall line (G1) (Fig. 14a). The degree to which these two sources of alongline momentum are independent is difficult to establish but it is apparent they both generated a northerly flow component behind the convective line.

To estimate the strength of the surface winds resulting from the surface pressure gradient, we follow Garratt and Physick (1983) who showed that the actual wind may be approximated as a linear function of time when the computed geostrophic wind is on the order of 10^2 m s^{-1}. Using a Eulerian reference frame, this relationship is as follows:

$$V = V_0 - \int_0^T \frac{1}{\rho} \nabla p dt, \qquad (1)$$

where V is the horizontal wind vector, p is pressure, ρ is density, T is the time interval, and the subscript zero refers to the initial state.

To calculate the northerly-component, we examine the average, north–south pressure gradient a surface station near $y = 0$ would experience as the mesohigh passed by to the north. From Fig. 10 we estimate this pressure gradient acceleration to be of the order 10^{-2} kg m s^{-2}. The distance from the gust front to the leading edge of the observed wind maximum (along $y = 0$) is approximately 24 km. Using Eq. (1), Fig. 10c, and a advective speed of 20 m s^{-1}, we estimate that

$$v = -5 - 1\ [\text{m}^3\ \text{kg}^{-1}] \frac{100\ \text{Pa}}{10\,000\ \text{m}} \times 1200\ \text{s} \sim -17\ \text{m s}^{-1}.$$

The use of Eq. (1) in this example, leads to a slight underprediction of the observed flow (-20 m s^{-1}). This simplified calculation suggests the strongest northerly winds were primarily a response to the local surface pressure gradient. We note that the horizontal and vertical advective terms in the v-momentum equation would further decrease the predicted estimate since v is negative and decreases in magnitude toward the north (see Fig. 10c), and $\partial v/\partial z > 0$ (Fig. 4). To account for the observed maximum, these affects must be compensated by an increase in the pressure gradient associated with the passage of the mesolow located behind the line or the alongline momentum generated by the rotational component of flow associated with the supercell (Fig. 14a).

Because the wind maximum was well removed from the convective portion of the line, one may question the role of the convective organization in developing and maintaining the strong north–south surface pressure gradient. In general, the strength and areal coverage of a surface mesohigh may depend on several environmental and storm circulation controls such as available buoyancy, middle-level moisture, and the orientation of the updraft (e.g., Nicholls et al. 1988). It is apparent that conditions favorable to producing large cold pools, such as an upshear tilted updraft, may be inimical to the convection which is required to maintain the cold pool (Rotunno et al. 1988). Thus long-lived, convectively induced, severe surface winds, which reflect a response of the atmosphere to maintain strong pressure perturbations, necessarily result from a precarious balance between the various feedback mechanisms which affect both system longevity and the maintenance of the surface pressure perturbation.

In this case, the mesohigh was particularly vigorous (7 hPa) and closely resembled both the shape of the overlying stratiform cloud shield and the bow-shaped convective organization (compare Figs. 6b and 10a) suggesting it was mainly hydrostatically induced by cooling and loading associated with the precipitation process. From the hypsometric equation, and an assumed in cloud temperature representative of moist adiabatic descent from 65 kPa (using the 0230 UTC aircraft sounding), we estimate that a 1 hPa surface pressure rise corresponds to a layer depth of approximately 400 m, viz.,

$$z = \frac{\delta p_0}{p_0} \frac{R\overline{T_v}^2}{g\Delta T_v} = \frac{100\ \text{Pa}}{91\,500\ \text{Pa}} 28.7\ [\text{K}^{-1}\ \text{m}] \times \frac{280^2\ \text{K}^2}{6\ \text{K}} = 410\ \text{m} \qquad (2)$$

To account for the 7 hPa pressure rise hydrostatically, would require a cold layer depth of roughly 2900 m over the northern portion of the mesonet. We infer from this analysis that the sloping $v = 0$ interface, evident in the Doppler radar analysis, resulted from a similar configuration of the cold air dome associated

[4] Strong wind gusts were certainly associated with the gust front passage (see Fig. 11 near 0239 UTC) but these gusts were not resolved in the five minute averaging used to construct the analyses presented in Fig. 10.

with the surface mesohigh. Compared to numerically produced cold pools, the depth of this cold pool would appear to be extreme but it may not be atypical of cold domes associated with squall lines embedded within MCCs (Ogura and Liou 1980).

The northward bias in the surface high pressure field was likely a result of the flow emanating from the supercell (G1), which would have preferentially deposited precipitation particles to the north (Fig. 14c), and residual convective debris associated with B1. We suggest the north–south surface pressure gradient was intensified by a hydrostatic reduction in pressure associated with middle-level subsidence accompanying the rear-to-front flow. Similar reasoning has been used to explain the wake mesolow with more linear two-dimensional systems (Johnson and Hamilton 1988). What may distinguish this system from linear squall lines, is the alongline variation evident in the rear-to-front flow. The deepest penetration occurred locally near the vertex of the bow echo (Fig. 16) where there was a corresponding minimum of the trough-to-ridge distance in the surface pressure distribution (see Fig. 10a near $y = 0$). The alongline variation in the middle-level subsidence may have been an important mechanism for maintaining the north–south pressure gradient which produced the strong northerly surface winds behind this squall line.

Another factor relevant to this storm, was the up/down downdraft component evident in the trajectories shown in Fig. 15. The characteristics of these trajectories reflect the stability of the presquall environment which was thermodynamically conducive to downdrafts if the initial lifting along the gust front was insufficient to propel the parcels beyond the level of free convection. The parcels near the supercell would experience the greatest lift (i.e., Rotunno and Klemp 1982) and would thus generate the potential for the strongest downdrafts once they moved out of the upward directed vertical pressure gradient force or encountered water loading, melting, and evaporation in the heavy precipitation process.

The up/down air parcel trajectories, such as A in Fig. 15, approached the surface wind maximum in a cyclonic fashion after descending in the primary downdraft on G1's northern flank. Because these parcels entered the storm from the east, against the low-level pressure field of the mesohigh, their net movement was likely a response to the rotational component of the supercell. As the parcels passed to the west side of the supercell, where they no longer opposed the surface pressure gradient, the momentum acquired during the down phase of the up/down downdraft could then enhance the northerly surface flow associated with the mesohigh.

It is evident by comparing Fig. 14a and Fig. 10a that the strongest northerly surface flow occurred where the rotation associated with the supercell likewise produced an alongline flow component. The wind maximum bulged forward on the southern flank of the supercell where again the rotational flow was in phase with the mesoscale flow produced by the mesohigh (Fig. 10b). This bulging forward of the wind maximum is thought to account for the bow echo shape, though in this case, it resulted from a considerably more complex sequence of events than envisioned, for example, by Fujita (1981). It appears that momentum generated on the convective-scale, may have locally enhanced the flow generated by the mesohigh near the observed surface wind maximum associated with this squall line. This may have accounted for the observed tendency of the wind to be locally strongest near the path taken by G1 (Fig. 1), rather than the more random distribution of surface wind gusts that may be expected with the passage of more linear systems.

7. Summary

In the presence of a stably stratified presquall ABL, this squall line readily produced intense surface outflow and strong convective updrafts. The strongest surface winds were located several kilometers behind the narrow convective band of this squall line where the flow was northerly or nearly parallel to the line. By considering a simplified momentum equation, it was shown that these characteristics could have been a result of accelerations caused by the local surface pressure gradient associated with a mesohigh–mesolow couplet.

The two-dimensional appearance of the "rear inflow jet" in the vertical cross sections, suggested that middle-level momentum may also have been transported toward the leading convective line. By considering the trajectory and surface θ_e analysis, we find that parcels within this circulation branch generally did not approach the convective line. Rather, they acquired a northerly flow component upon encountering the $v < 0$ wedge and exited to the rear of the system. This suggests that the middle-level momentum was strongly modified as it descended through the lower levels of the line segment by the near surface pressure field. Thus we feel that conclusions drawn from two-dimensional cross-sections depicting squall line flow fields may be misleading if not accompanied by trajectory calculations to determine the source and destination regions of the air parcels within the cross section.

This line segment showed considerable alongline variation in both the surface kinematic fields and the radar-derived precipitation and flow fields. We attribute the three dimensional characteristics to the presence of the supercell G1. This was the dominant cell group within the line segment and was a well-defined reflectivity maximum that could be tracked by radar for several hours. This behavior, which is atypical for tropical and many middle latitude squall lines, presumably resulted from deep, strong shear, which favored the

formation of a quasi-steady cell (e.g., Rotunno and Klemp 1985). This case illustrates that a squall line residing in such an environment can be composed of both ordinary cells and rotating, quasi-steady cells. It also illustrates that convective systems associated with stable ABLs, are capable of producing damaging winds without invoking conservation of middle-level momentum arguments.

Acknowledgments. The authors are indebted to Kevin Knupp for numerous discussions and guidance in completing the Doppler analyses. The constructive comments made by reviewers M. S. Fritsch and M. Moncrief along with an anonymous reviewer greatly improved the manuscript. Ray McAnelly is also acknowledged for his generous support in providing several of the figures presented here and for reviewing the manuscript. Carl Mohr is recognized for his assistance with our use of the Cedric software analysis package. The trajectory programs were provided by JoAnn Parrish of NCAR and the Wyoming King Air data by Marcia Politovich from the University of Wyoming. Additional wind reports were received by Robert H. Johns of the National Severe Storms Forecasting Center. Brenda Thompson assisted in the preparation of the manuscript and the figures were drafted Lucy McCall. This research was supported by the National Science Foundation under Grant ATM-8512480. Computer analysis of the Doppler radar data was performed on the NCAR CRAY-XMP. NCAR is supported by the National Science Foundation.

REFERENCES

Brunk, I. W., 1949: The pressure pulsation of April 11, 1944. *J. Meteor.*, **6**, 395–401.

Browning, K. A., 1977: The structure and mechanisms of hailstorms. *Meteor. Monogr.*, No. 38, 1–43.

Chong, M., P. Amayene, G. Scialom and J. Testud, 1987: A tropical squall line observed during the COPT 81 experiment in West Africa. Part I: Kinematic structure inferred from dual-Doppler radar data. *Mon. Wea. Rev.*, **115**, 670–694.

Foote, G. B., and H. W. Frank, 1983: Case study of a hailstorm in Colorado. Part III: Airflow from triple-Doppler measurements. *J. Atmos. Sci.*, **40**, 686–707.

Frank, W. M., and G. B. Foote, 1982: The 22 July 1976 case study: Storm airflow, up-draft structure, and mass flux from triple-Doppler measurements. *Hailstorms of the Central High Plains.* Vol. 2, Colorado Associated University Press, 131–162.

Fujita, T. T., 1955: Results of detailed synoptic studies of squall lines. *Tellus*, **7**, 405–434.

——, 1981: Tornadoes and downbursts in the context of generalized planetary scales. *J. Atmos. Sci.*, **38**, 1511–1534.

Gal-Chen, Tzvi, 1982: Errors in fixed and moving frame of references: Applications for conventional and Doppler radar analysis. *J. Atmos. Sci.*, **39**, 2279–2300.

Gamache, J. F., and R. A. Houze, Jr., 1982: Mesoscale air motions associated with a tropical squall line. *Mon. Wea. Rev.*, **110**, 118–135.

Garratt, J. R., and W. L. Physick, 1983: Low-level wind response to mesoscale pressure systems. *Bound.-Layer Meteor.*, **27**, 69–87.

Green, R., and M. Kruidenier, 1982: Interactive data processing for mesoscale forecasting applications. *Proc. Ninth Conf. on Weather Forecasting and Analysis*, Seattle, Amer. Meteor. Soc., 60–62.

Hane, C. E., 1973: The squall line thunderstorm: numerical experimentation. *J. Atmos. Sci.*, **30**, 1672–1690.

Hinrichs, G., 1888: Tornadoes and derechos. *Amer. Meteor. J.*, **5**, 306–317, 341–349.

Houze, R. A., Jr., 1977: Structure and dynamics of a tropical squall-line system. *Mon. Wea. Rev.*, **105**, 1540–1567.

——, and E. N. Rappaport, 1986: Air motions and precipitation structure of an early summer squall line over the eastern tropical Atlantic. *J. Atmos. Sci.*, **41**, 553–573.

James, P. K., and K. A. Browning, 1979: Mesoscale structure of line convection at surface cold fronts. *Quart. J. Roy. Meteor. Soc.*, **105**, 371–382.

Johns, R. H., and W. D. Hirt, 1987: Derechos: Widespread convectively induced windstorms. *Wea. Forecasting*, **2**, 32–49.

Johnson, R. H., and P. J. Hamilton, 1988: The relationship of surface pressure features to the precipitation and air flow structure of an intense midlatitude squall line. *Mon. Wea. Rev.*, **116**, 1444–1472.

Knight, C. A., 1982: The Cooperative Convective Precipitation Experiment (CCOPE), 18 May–78 August 1981. *Bull. Amer. Meteor. Soc.*, **63**, 386–398.

Knupp, K. R., 1987: Downdrafts within High Plains Cumulonimbi. Part I: General kinematic structure. *J. Atmos. Sci.*, **44**, 987–1008.

Lilly, D. K., 1979: The dynamical structure and evolution of thunderstorms and squall lines. *Annu. Rev. Earth Planet Sci.*, **7**, 117–161.

Maddox, R. A., 1980: Mesoscale convective complexes. *Bull. Amer. Meteor. Soc.*, **61**, 1374–1387.

Marwitz, J. D., 1972: The structure and motion of severe hailstorms. Part I: Supercell storms. *J. Appl. Meteor.*, **11**, 166–179.

——, 1973: Trajectories within the weak echo regions of hailstorms. *J. Appl. Meteor.*, **12**, 1174–1182.

Miller, L. J., C. G. Mohr and A. J. Weinheimer, 1986: The simple rectification to cartesian space of folded radical velocities from Doppler radar sampling. *J. Atmos. Oceanic Technol.*, **3**, 162–174.

——, J. D. Tuttle and C. A. Knight, 1988: Airflow and hail growth in a severe northern High Plains supercell. *J. Atmos. Sci.*, **45**, 736–762.

Mohr, C. G., L. J. Miller, R. L. Vaughn and H. W. Frank, 1986: The merger of mesoscale datasets into a common cartesian format for efficient and systematic analyses. *J. Atmos. Oceanic Technol.*, **3**, 143–161.

Newton, C. W., 1950: Structure and mechanism of the prefrontal squall line. *J. Meteor.*, **8**, 210–222.

——, 1966: Circulations in large sheared cumulonimbus. *Tellus*, **18**, 699–713.

Nicholls, M. E., R. H. Johnson and W. R. Cotton, 1988: The sensitivity of two-dimensional simulations of tropical squall lines to environmental profiles. *J. Atmos. Sci.*, **45**, 3625–3649.

Nolen, R. H., 1959: A radar pattern associated with tornadoes. *Bull. Amer. Meteor. Soc.*, **40**, 277–279.

Ogura, Y., and M. T. Liou, 1980: The structure of a midlatitude squall line: A case study. *J. Atmos. Sci.*, **37**, 553–567.

Parrish, J. L., and A. J. Heymsfield, 1985: A user guide to a particle growth and trajectory model (using one-dimensional and three-dimensional wind fields). NCAR Tech. Note NCAR/Tn-259+IA, 69 pp.

Rotunno, R., and J. B. Klemp, 1982: The influence of shear-induced pressure gradients on thunderstorm motion. *Mon. Wea. Rev.*, **110**, 136–151.

——, and ——, 1985: On the rotation and propagation of simulated supercell thunderstorms. *J. Atmos. Sci.*, **42**, 271–292.

——, —— and M. L. Weisman, 1988: A theory for strong, long-lived squall lines. *J. Atmos. Sci.*, **45**, 463–485.

Seitter, K. L., and H. L. Kuo, 1983: The dynamical structure of squall-line type thunderstorms. *J. Atmos. Sci.*, **40,** 2831–2854.

Smull, B. F., and R. A. Houze, Jr., 1987: Rear inflow in squall lines with trailing stratiform precipitation. *Mon. Wea. Rev.*, **115,** 2869–2889.

Srivastava, R. C., T. J. Matejka and T. J. Lorello, 1986: Doppler radar study of the trailing anvil region associated with a squall line. *J. Atmos. Sci.*, **43,** 356–377.

Thorpe, A. J., M. J. Miller and M. W. Moncrieff, 1982: Two-dimensional convection in nonconstant shear: A model of mid-latitude squall lines. *Quart. J. Roy. Meteor. Soc.*, **108,** 739–762.

Wade, C. G., 1982: A preliminary study of an intense thunderstorm which moved across the CCOPE research network in Southeastern Montana. Preprints, *Ninth Conf. on Weather Forecasting and Analysis*, Seattle, 388–395.

Weisman, M., and J. Klemp, 1982: The dependence of numerically simulated convective storms on vertical wind shear and buoyancy. *Mon. Wea. Rev.*, **110,** 504–520.

——, and ——, 1984: The structure and classification of numerically simulated convective storms in directionally varying wind shears. *Mon. Wea. Rev.*, **112,** 2479–2498.

——, —— and L. J. Miller, 1983: Modeling and Doppler analysis of the CCOPE August 2 supercell storm. Preprints, *13th Conf. on Severe Local Storms*, Amer. Meteor. Soc., 223–226.

Wexler, R., 1947: Radar detection of a frontal storm 18 June 1946. *J. Meteor.*, **4,** 38–44.

Zipser, E. J., 1969: The role of organized unsaturated convective downdrafts in the structure and rapid decay of an equitorial disturbance. *J. Appl. Meteor.*, **8,** 799–814.